



Calhoun: The NPS Institutional Archive
DSpace Repository

Theses and Dissertations

1. Thesis and Dissertation Collection, all items

2004-03

Multiple beam directors for naval free electron laser weapons

Mitchell, Ethan D.

Monterey California. Naval Postgraduate School

<http://hdl.handle.net/10945/1645>

This publication is a work of the U.S. Government as defined in Title 17, United States Code, Section 101. Copyright protection is not available for this work in the United States.

Downloaded from NPS Archive: Calhoun



Calhoun is the Naval Postgraduate School's public access digital repository for research materials and institutional publications created by the NPS community. Calhoun is named for Professor of Mathematics Guy K. Calhoun, NPS's first appointed -- and published -- scholarly author.

Dudley Knox Library / Naval Postgraduate School
411 Dyer Road / 1 University Circle
Monterey, California USA 93943

<http://www.nps.edu/library>



NAVAL POSTGRADUATE SCHOOL

MONTEREY, CALIFORNIA

THESIS

**MULTIPLE BEAM DIRECTORS FOR NAVAL FREE
ELECTRON LASER WEAPONS**

by

Ethan D. Mitchell

March 2004

Thesis Advisor:
Co-Advisor:

William Colson
Joseph Blau

Approved for Public Release; Distribution is Unlimited

THIS PAGE INTENTIONALLY LEFT BLANK

REPORT DOCUMENTATION PAGE			<i>Form Approved OMB No. 0704-0188</i>	
Public reporting burden for this collection of information is estimated to average 1 hour per response, including the time for reviewing instruction, searching existing data sources, gathering and maintaining the data needed, and completing and reviewing the collection of information. Send comments regarding this burden estimate or any other aspect of this collection of information, including suggestions for reducing this burden, to Washington headquarters Services, Directorate for Information Operations and Reports, 1215 Jefferson Davis Highway, Suite 1204, Arlington, VA 22202-4302, and to the Office of Management and Budget, Paperwork Reduction Project (0704-0188) Washington DC 20503.				
1. AGENCY USE ONLY (Leave blank)		2. REPORT DATE March 2004	3. REPORT TYPE AND DATES COVERED Master's Thesis	
4. TITLE AND SUBTITLE: Multiple Beam Directors for Naval Free Electron Laser Weapons			5. FUNDING NUMBERS	
6. AUTHOR(S) Mitchell, Ethan D.				
7. PERFORMING ORGANIZATION NAME(S) AND ADDRESS(ES) Naval Postgraduate School Monterey, CA 93943-5000			8. PERFORMING ORGANIZATION REPORT NUMBER	
9. SPONSORING /MONITORING AGENCY NAME(S) AND ADDRESS(ES) N/A			10. SPONSORING/MONITORING AGENCY REPORT NUMBER	
11. SUPPLEMENTARY NOTES The views expressed in this thesis are those of the author and do not reflect the official policy or position of the Department of Defense or the U.S. Government.				
12a. DISTRIBUTION / AVAILABILITY STATEMENT Approved for public release; distribution is unlimited.			12b. DISTRIBUTION CODE	
13. ABSTRACT (maximum 200 words) The Free Electron Laser has the potential to become a revolutionary weapon system. Deep magazines, low cost-per-shot, pinpoint accuracy, and speed of light delivery give this developing weapon system significant advantages over conventional systems. One limiting factor in high energy laser implementation is thermal blooming, a lensing effect which is caused by the quick heating of the atmosphere, so that the laser beam does not focus on the desired spot, thereby degrading the effectiveness of the laser on target. The topic of this thesis was to study the use of multiple beam directors focusing on a target from a single platform, which may mitigate thermal blooming by allowing half of the laser's energy to travel through a given volume of air, so that they only overlap very near the target. Less energy traveling through a given volume of space means less heating, and therefore lessens the effects of thermal blooming. Also, simulations of FEL's were conducted modifying parameters such as the number of undulator periods, electron beam focus, the normalized Rayleigh length, and mirror output coupling, in order to determine optimum design parameters. New parameters for the next proposed FEL were simulated to examine the effect of mirror tilt on laser power and extraction as well.				
14. SUBJECT TERMS Free Electron Laser, Short Rayleigh Length, Directed Energy, Thermal Blooming, Multiple Beam Directors			15. NUMBER OF PAGES 82	
			16. PRICE CODE	
17. SECURITY CLASSIFICATION OF REPORT Unclassified	18. SECURITY CLASSIFICATION OF THIS PAGE Unclassified	19. SECURITY CLASSIFICATION OF ABSTRACT Unclassified	20. LIMITATION OF ABSTRACT UL	

THIS PAGE INTENTIONALLY LEFT BLANK

Approved for public release; distribution is unlimited.

**MULTIPLE BEAM DIRECTORS FOR NAVAL FREE ELECTRON LASER
WEAPONS**

Ethan D. Mitchell
Lieutenant, United States Navy
B.S., United States Naval Academy, 1997

Submitted in partial fulfillment of the
requirements for the degree of

MASTER OF SCIENCE IN PHYSICS

from the

**NAVAL POSTGRADUATE SCHOOL
March 2004**

Author: Ethan D. Mitchell

Approved by: William B. Colson
Thesis Advisor

Joseph A. Blau
Co-Advisor

James H. Luscombe
Chairman, Department of Physics

THIS PAGE INTENTIONALLY LEFT BLANK

ABSTRACT

The Free Electron Laser has the potential to become a revolutionary weapon system. Deep magazines, low cost-per-shot, pinpoint accuracy, and speed of light delivery give this developing weapon system significant advantages over conventional systems. One limiting factor in high energy laser implementation is thermal blooming, a lensing effect which is caused by the quick heating of the atmosphere, so that the laser beam does not focus on the desired spot, thereby degrading the effectiveness of the laser on target. The use of multiple beam directors focusing on a target from a single platform may mitigate thermal blooming by allowing half of the laser's energy to travel through a given volume of air, so that they only overlap very near the target. Less energy traveling through a given volume of space means less heating, and therefore lessens the effects of thermal blooming. Also, simulations of FEL's were conducted modifying parameters such as the number of undulator periods, electron beam focus, the normalized Rayleigh length, and mirror output coupling, in order to determine optimum design parameters. New parameters for the next proposed FEL were simulated to examine the effect of mirror tilt on laser power and extraction as well.

THIS PAGE INTENTIONALLY LEFT BLANK

TABLE OF CONTENTS

I.	INTRODUCTION	1
A.	JUSTIFICATION FOR THE FREE ELECTRON LASER (FEL)	1
1.	Laser Applications in the Navy.....	1
2.	Advantages of the FEL Over Other Laser Technologies	4
B.	THESIS CONTENTS	5
II.	THEORY	7
A.	BASIC FEL DESCRIPTION.....	7
B.	UNDULATOR FIELDS AND THE RESONANCE CONDITION.....	8
C.	ELECTRON MOTION	11
D.	THE OPTICAL WAVE EQUATION.....	16
E.	GAIN	19
F.	PHASE SPACE	22
III.	MULTIPLE BEAM DIRECTORS	25
A.	DISCUSSION	26
B.	EFFECT OF DISTANCE ALONG BEAM OF THERMAL BLOOMING.....	28
1.	Simulation Methods.....	28
2.	Simulation Results	29
C.	GEOMETRIC DERIVATION OF BEAM OVERLAP	32
D.	PLACEMENT OPTIONS FOR TWO DIRECTORS.....	34
IV.	SIMULATIONS OF THE SHORT RAYLEIGH LENGTH FEL	39
A.	SINGLE-MODE SIMULATIONS	40
B.	MULTIMODE SIMULATIONS	43
C.	SIMULATION RESULTS	45
1.	Variation of Undulator Length and Position.....	45
2.	Variation of Electron Beam Focus	47
3.	Variation of the Rayleigh Length z_0	49
4.	Variation of Mirror Output Coupling Q_n	50
D.	MIRROR TILT	51
1.	Extraction Decrease Due to Beam Tilt.....	52
2.	Mode Shape	53
V.	CONCLUSION	57
	LIST OF REFERENCES.....	59
	INITIAL DISTRIBUTION LIST	61

THIS PAGE INTENTIONALLY LEFT BLANK

LIST OF FIGURES

Figure 1.	Canopy Glazing by Laser.....	3
Figure 2.	Undulator and Resonator Cavity.....	7
Figure 3.	Electron-Photon Race	9
Figure 4.	Phase Space Plot for Electrons on Resonance	22
Figure 5.	Phase Space Plot With $v_0=2.6$	23
Figure 6.	Transmittance of 1000 ft horizontal path at sea level at 79°F containing 5.7nm precipitable water [13]	25
Figure 7.	Conceptual laser beam director.....	27
Figure 8.	Firing arcs for directors placed fore and aft.....	27
Figure 9.	Beam propagation with no thermal blooming.	29
Figure 10.	Stagnation zone at (a) 30%, (b) 50% and (c) 80% of total range.	30
Figure 11.	Positioning of the stagnation zone for varying strength of the zone.....	31
Figure 12.	3-D plot of stagnation zone placement and strength.....	32
Figure 13.	Overlap of beams at target.....	33
Figure 14.	Triangular representation of beam overlap.....	33
Figure 15.	Overlapping volume.....	34
Figure 16.	Percent overlap of two beam directors.....	35
Figure 17.	Overlap volume for two directors.....	36
Figure 18.	Optical and electron beam focusing in undulator.	39
Figure 19.	Single-mode simulation sample output.....	42
Figure 20.	Multimode simulation output.....	44
Figure 21.	Results of varying undulator periods.....	47
Figure 22.	Pictorial representation of electron focusing.	47
Figure 23.	(a) Strong and (b) weak electron beam focusing.....	48
Figure 24.	Variation of electron beam waist radius r_b	49
Figure 25.	Variation of the Rayleigh length.....	50
Figure 26.	Variation of mirror output coupling Q_n	51
Figure 27.	Multimode simulation run with tilted mirrors.	52
Figure 28.	Extraction decrease due to mirror tilt.....	53
Figure 29.	Example of finding maximum extraction varying initial electron phase velocity.....	53
Figure 30.	Optical mode profiles for $z_0 = 0.03$, $\theta_m = 0.01$, and $v_0 =$ (a) 8.0, (b)8.5, and (c)10.....	54

THIS PAGE INTENTIONALLY LEFT BLANK

LIST OF TABLES

Table 1.	Simulation parameters.	40
----------	-----------------------------	----

THIS PAGE INTENTIONALLY LEFT BLANK

ACKNOWLEDGMENTS

I would like to thank Prof. Colson, Prof. Armstead, and Prof. Blau for their frank and helpful advice in writing this thesis. Your support and understanding was invaluable in bringing what first seemed an insurmountable task into perspective. Thank you also for not laughing when I suggested this topic, letting me pursue it, and actually seeming genuinely interested in the results.

I would like thank the Physics Faculty here at NPS for rekindling my curiosity in science. The more I learned, the more fascinating it became, and the more I wanted to know. This renewed desire for understanding the world around me is probably one of the greatest gifts I could have received.

To the guys in the office, thanks for helping me keep in mind the small stuff that makes life fun, like ballistic water (and ammonia) bottles. Also for teaching me our most important role in physics conventions, which is, of course, taking Physicists to bars.

I would like to thank my mother for her belief in me and all her help in making me who I am today. You did an incredible job, and I cannot thank you enough. To my brother, who is living proof that true education does not require fancy pieces of paper, I just wanted to say for the record that I am proud of you.

Finally, to my wife, I wanted to say thank you for your unwavering support. You have made everything possible. I love you. To my son, watching you grow over the past ten months has been more amazing than can be expressed in words. I had never realized how much happiness one little smile can bring.

THIS PAGE INTENTIONALLY LEFT BLANK

LIST OF SYMBOLS

a	complex dimensionless optical field
a_0	dimensionless optical field strength at $\tau = 0$
a_1	dimensionless optical field strength at $\tau = 1$
$ a $	optical field amplitude
A	area of beam spot on target
A	optical mode area
A_0	area of beam spot on target unaffected by thermal blooming
\mathbf{A}	vector potential
B	undulator magnetic field magnitude
\mathbf{B}	vector sum of optical and magnetic fields
\mathbf{B}_s	optical magnetic field
\mathbf{B}_u	undulator magnetic field
c	speed of light
e	charge of an electron
E	optical field magnitude
E_e	electron energy
\mathbf{E}_s	optical electric field
F	filling factor
G	gain
h	height of beam
I_{peak}	peak current
I_{avg}	average current
j	dimensionless current density
\mathbf{J}_{\perp}	transverse current density
k	optical wave number
k_0	undulator wave number
K	dimensionless undulator parameter
l_0	length of beam overlap
l_p	length of beam before touching
l_b	bunch length
l_t	distance from ship to target
L	undulator length
m	electron mass
n	number of passes
N	number of undulator periods
N_e	number of electrons
\mathbf{r}_i	radial position of i^{th} electron
r_b	electron beam focal width
r_c	dimensionless resonator cavity mirror curvature
r_m	dimensionless resonator cavity mirror radius
r_s	radius of beam at source
r_t	radius of beam at target

S	resonator length
t	time
\mathbf{v}	relativistic electron velocity
v_z	electron longitudinal velocity
V	volume
w_0	optical waist radius
w	optical beam radius at mirror
x_s	horizontal separation of beam directors
x_\perp	transverse electron position
z	longitudinal distance along undulator
z_b	electron beam focal position
z_0	Rayleigh length
β	non-dimensional electron velocity (\mathbf{v}/c)
β_\perp	electron transverse velocity
β_z	longitudinal velocity of electron
$\delta^3(\mathbf{x}-\mathbf{r}_i)$	three dimensional Dirac delta function
ε_m	emittance
$\hat{\varepsilon}_1$	unit vector = $(\cos \psi, -\sin \psi, 0)$
$\hat{\varepsilon}_2$	unit vector = $(-\sin \psi, -\cos \psi, 0)$
γ	Lorentz factor
η	extraction
ψ	optical phase
λ	optical wavelength
λ_0	undulator wavelength
v	dimensionless electron phase velocity
ρ_e	electron density
σ	dimensionless electron beam radius
θ	resonator mirror tilt
θ_m	dimensionless mirror tilt
$\theta_{x,y,z}$	angular spread of electrons
τ	dimensionless time
τ_β	dimensionless beam focus
τ_w	optical mode waist position
τ_r	dimensionless time along range to target
τ_c	location of stagnation zone along τ_r
ω	optical frequency
ω_0	undulator frequency
ω_β	betatron frequency
$d\phi_s$	effective stagnation zone strength
ϕ	initial optical phase
ζ	electron phase

$(\dots)^{\cdot}$	first time derivative
$(\dots)^{\ddot{}}$	second time derivative
$(\dots)^{\circ}$	first dimensionless time derivative
$(\dots)^{\circ\circ}$	second dimensionless time derivative
$(\dots)'$	first spatial derivative
$\langle \dots \rangle$	time average

THIS PAGE INTENTIONALLY LEFT BLANK

I. INTRODUCTION

A. JUSTIFICATION FOR THE FREE ELECTRON LASER (FEL)

Over the history of naval warfare, there have been certain technological developments that have been touted as revolutions in military affairs. Among these can be included the use of the sail, canons, steam power, metal hulls, and the evolution of missile and radar technology. The next step in the evolution of naval warfare may be the use of electric weapons, such as lasers and rail guns. A strong contender for naval application of directed energy is the free electron laser. It has countless applications and advantages over other laser technologies, which will be discussed in this section.

1. Laser Applications in the Navy

Lasers have many applications in the maritime arena. The first and most prominent is their use in anti-ship cruise missile defense. Self-defense weapons, such as the CIWS (Close-In Weapon System) and RAM (Rolling Airframe Missile), currently in the U.S. arsenal are insufficient. Both have very limited range, difficulties intercepting maneuvering missiles, and limited magazines. Lasers possess the potential to have much longer ranges, virtually bottomless magazines, and fewer complications when attacking a maneuvering target.

The laser's range is limited by the line of sight, making ranges of 8 to 10 nm possible in good weather. The CIWS has a range of less than 2 nm and the RAM 6 nm. The laser adds to this range advantage the capability of zero flight time. Because the laser propagates at the speed of light, the effect begins instantaneously, whereas for the other systems, there is a significant delay between launch and intercept. This delay between engagement and kill can be deadly, as it leaves little reaction time to fire additional salvos if the first is ineffective.

The term "bottomless magazine" is applied to electric lasers because they do not use conventional ammunition. Electric laser technologies are limited only by the electricity sent to it, which depends on the ship's electrical power available. As long as the ship has the fuel to supply electric power to the laser, the laser operates.

Lasers are expected to be much more effective against high-speed targets capable of high-G turns. This is because there is no longer the need to lead the target. With current conventional weapon systems, there is the aforementioned time lag between the time a round is fired and when it makes contact with the target. As such, the weapon system must lead the target, shooting where it predicts the target to be once the rounds meet the missile. If, however, the missile makes too many maneuvers during this intervening time, the rounds can miss. Similarly, when using missiles, the missile must attempt to hit a target missile moving at an incredibly high relative speed. If the target missile maneuvers, it is difficult for the missile tracking it to maneuver quickly enough to destroy it. The advantage of speed-of-light-delivery is that all of these considerations are now insignificant. The laser director needs only to adjust the tilt of a mirror to maintain track, and does not need to attempt to lead the target. No matter what the target missile does, it cannot out-maneuver the laser.

There are numerous other applications for lasers in the military. One of these is a capability which the current arsenal is lacking, the “soft kill”. A soft kill is when a system is rendered ineffective due to means other than the actual structural damage usually associated with weapon systems. The laser can accomplish many variations of the soft kill. One is sensor blinding, in which the target’s means of detection and tracking are disabled. The laser can accomplish this by overloading optical circuits or destroying key electronic components. Another is glazing, in which the laser is aimed at a glass surface and the interaction causes the glass to cloud as in Figure 1 below. This can be extremely effective against aircraft cockpits. A third method of soft kill is the ability to disable vehicle engines. Lasers can pin-point specific areas of vehicles and burn through the body in order to destroy key engine components, especially electrical components such as spark plug wires.



Figure 1. Canopy Glazing by Laser

This capability leads to another aspect of the laser that far surpasses any weapon currently in the inventory, minimum collateral damage. In today's conflicts, there is an emphasis on accuracy. This has led to the implementation of precision-guided bombs as the munitions of choice. As accurate as is current laser and GPS guiding technology, there is still a delicate balance that must be maintained. An explosive should be minimized and the blast aimed in order to minimize collateral damage, but still large enough to produce the desired lethality. There is a limit on how precise an explosive can be due to the blast effects. With lasers, the energy is localized on a small area of the target, so that there is little effect outside of the aim point. This allows for unprecedented accuracy and minimal damage outside of the desired area.

Finally, there are applications for the laser in the field of ship's self defense. This applies to such scenarios as swarm raids, in which an adversary uses a large number of small boats such as speed boats or jet skis armed with hand held rockets and small arms in order to overwhelm the ship's defenses. Currently, ships are equipped with a few .50 caliber machine guns and perhaps a 20mm chain gun. Cruisers and destroyers also have their 5" gun mounts. Fire hoses are used to repel boarders. All of these systems are inaccurate and difficult to use against such high-speed threats, and there is slow transition from one target to the next. A laser would not be affected by the high-speed maneuvers of which these platforms are capable for the same reasons that it is not affected by missiles' maneuverability. The laser's accuracy, speed of light delivery, and ability to quickly shift from target to target are immeasurably better than those currently in use.

This aspect of the laser's potential use, as well as the minimum collateral damage and soft kill capability, can also be applied to unknown threats approaching a ship. Currently, the ship's force has few options other than lethal force to defend itself. In the current world climate, threats are not usually well defined. As evidenced by the USS Cole incident, there is little a ship can do but wait to find out the intentions of an approaching unidentified vessel. If lethal force were used to deter an approaching vessel that had not identified itself, the ramifications would be severe if it was a civilian. Lasers would allow ship's force to disable an approaching vessel whose threat status could not be determined.

2. Advantages of the FEL Over Other Laser Technologies

The FEL has many advantages over the other laser technologies, solid-state and chemical, available today. These include scalability, the property of being tunable, and the lack of hazardous chemicals and materials as output products.

Free Electron Lasers are currently the most scalable lasers available. The potential for mega-watt operation is much more feasible for FEL's than any other medium. This is primarily because the lasing medium is a vacuum. In all other lasers, there is a medium in which lasing occurs that must be cooled, and this puts a significant constraint on the amount of power that can be achieved. In solid state lasers, there is a solid crystalline medium through which the laser beam must propagate in order to increase its power. Absorption can significantly heat the material, so that it must be cooled. Because of the solid nature of this material, the heat must be conducted out, which is limited by the surface area that can be reached by the cooling medium.

With a chemical laser, this lasing medium is exhausted, and the heat carried out with this exhaust. While this seems to mitigate the cooling problem, this exhaust gas is highly toxic and corrosive. In a ship-board environment, this exhaust is very difficult to direct such that it is not detrimental to personnel and equipment. Also, the storage of these lasing gases is a serious issue, since the chemicals are toxic and corrosive before reacting as well.

A tunable FEL means that it has the capability of changing the wavelength of the light emitted, or tuning, as required, without significantly impacting the design of the

laser. Solid state and chemical lasers depend upon the materials used to determine their operational wavelength. In order for solid state or chemical lasers to lase at different wavelengths, new mediums must be found with the appropriate properties, and the whole laser effectively redesigned. Tunability is useful because the atmosphere absorbs some wavelengths of electromagnetic radiation, while allowing others to pass relatively unaffected. Due to its ability to adjust the wavelength with little impact on design, FEL designers can look for what wavelengths best propagate through the atmosphere, and build the appropriate design to best take advantage of these windows.

B. THESIS CONTENTS

This thesis will begin by discussing the theory behind a free electron laser. It will then discuss a possible solution to thermal blooming, which is a prominent limiting factor in high energy laser implementation. Thermal blooming is a lensing effect which is caused by the quick heating of the atmosphere, so that the laser beam does not focus on the desired spot, thereby degrading the effectiveness of the laser on target. This potential solution is the use of multiple beam directors from a single platform to focus on a target. This may mitigate thermal blooming by allowing half of the laser's energy to travel through a given volume of air, so that they only overlap very near the target. Less energy traveling through a given volume of space means less heating, and therefore lessens the effects of thermal blooming.

Also, simulations of FEL's were conducted modifying parameters such as the number of undulator periods, electron beam focus, the normalized Rayleigh length, and mirror output coupling, in order to determine optimum design parameters. Simulations were also conducted in order to examine the effect of mirror tilt on laser power and extraction.

THIS PAGE INTENTIONALLY LEFT BLANK

II. THEORY

A. BASIC FEL DESCRIPTION

The Free Electron Laser may be described in completely classical, as opposed to quantum-mechanical, terms. It is easy to explain qualitatively, but the quantitative physical description is challenging enough to be interesting. The FEL is based on the fact that accelerating electrons radiate energy. In order to achieve this, electrons are emitted from a cathode in discrete bunches. These are accelerated in an RF accelerator to relativistic velocities. These electrons are then sent into what is called an undulator, which contains a stationary magnetic field in a periodic transverse, spatial configuration. There are two primary types of undulator polarization, linear and helical. In a linear undulator, which is most common in today's FELs, there are two rows of magnets, between which the electrons pass. These magnets alternate polarities along the undulator, so that as the electron bunches pass along the undulator axis, they experience alternating forces, causing them to weave with a slalom type motion. This type of undulator is shown in Figure 2 with the electron path shown as the light blue line.

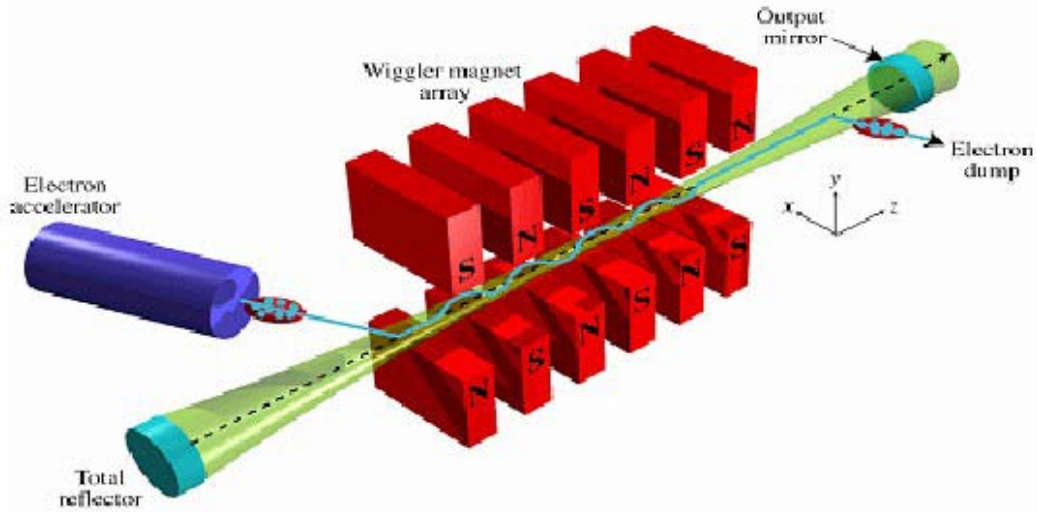


Figure 2. Undulator and Resonator Cavity

This slalom motion is caused by accelerating the electrons periodically in the direction transverse to the motion of the electrons. In general, the acceleration of moving charges in a magnetic field is caused by the Lorentz Force.

This acceleration causes the electrons to radiate along the axis of motion. This radiation is reflected off of the mirrors, which can be seen in Figure 2. The region between these mirrors is called the resonator cavity. One mirror is fully reflecting, while the other is partially transmissive. In the figure, the latter is the mirror on the right. The light that is transmitted through the right mirror is propagated to the target.

A helical undulator generates the magnetic field by wires wound around the central cavity in a spiral. In this configuration, the electrons see a field which rotates around the axis as they travel through the undulator. The theory of this type of undulator will be examined in the next sections.

The electrons are then decelerated through the same accelerator cavities in which they were accelerated by sending them through 180° out of phase. This offers two advantages. First, this deceleration significantly lowers the electrons' energy so that when they reach the beam dump, the radiation emitted by the electrons colliding with the dump is significantly decreased. Second, this allows for energy recovery. The decelerating electrons transfer the energy that they lose back to the electromagnetic fields, thus decreasing the amount of supplied energy that the fields need to accelerate the electrons. This can significantly increase the wall-plug efficiency of the FEL, potentially increasing a 100 kW laser from 2% to over 6%. [12]

B. UNDULATOR FIELDS AND THE RESONANCE CONDITION

Within the resonator cavity, there are three different electromagnetic fields which interact with the electrons. They are the optical magnetic field, symbolized by \mathbf{B}_s , the optical electric field, \mathbf{E}_s , and the undulator magnetic field, \mathbf{B}_u . These fields create forces on the electrons via the relativistic Lorentz equation, which in cgs units is

$$\frac{d}{dt}(\gamma\boldsymbol{\beta}) = -\frac{e}{mc}(\mathbf{E}_s + \boldsymbol{\beta} \times \mathbf{B}), \quad (2.1)$$

where $\mathbf{v} = \boldsymbol{\beta}c$ is the relativistic velocity of the electron, $|e|$ is the electron charge magnitude, m the electron mass, c the speed of light, $\mathbf{B} = \mathbf{B}_s + \mathbf{B}_u$, and

$$\gamma = \frac{1}{\sqrt{1 - \beta^2}} \quad (2.2)$$

is defined as the Lorentz Factor. The electron's energy is then $E_e = \gamma mc^2$, which typically is approximately 100 MeV, yielding a $\beta = 0.999986 \approx 1$, and $\gamma \approx 200$.

In a helical undulator, the above mentioned fields are given as

$$\mathbf{B}_s = E (\sin \psi, \cos \psi, 0), \quad (2.3)$$

$$\mathbf{E}_s = E (\cos \psi, -\sin \psi, 0), \text{ and} \quad (2.4)$$

$$\mathbf{B}_u = B (\cos(k_0 z), \sin(k_0 z), 0), \quad (2.5)$$

where E is the magnitude of the optical field, $\psi = kz - \omega t + \phi$, $k = 2\pi/\lambda$ is the optical wave number, λ is the optical wavelength, z is the longitudinal distance along the undulator, $\omega = kc$ is the optical frequency, ϕ is the optical phase, B is the magnitude of the undulator magnetic field, and $k_0 = 2\pi/\lambda_0$ is the undulator wave number with λ_0 the undulator wavelength.

Resonance is an important concept in the operation of the free electron laser. It is defined as the conditions under which exactly one wavelength of light passes over an electron in one undulator period. See Figure 3 below, in which the red circle is as electron, the blue line a wavelength of light, and the green line an undulator wavelength.

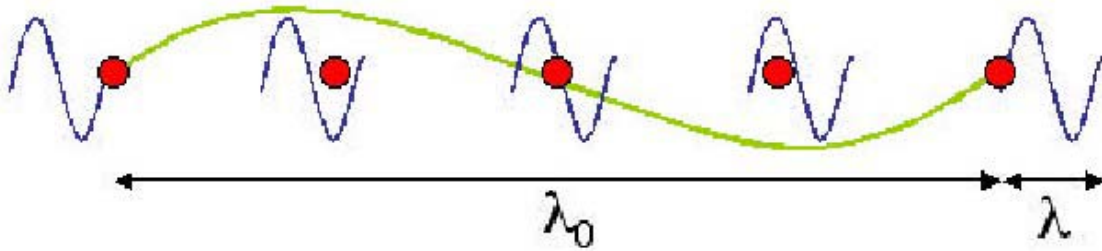


Figure 3. Electron-Photon Race

The resonance condition allows for determining the wavelength of light that is generated by a FEL. The time that it takes one electron to travel one undulator period is defined as Δt , and the velocity in the z direction of the electron is $v_z = \lambda_0/\Delta t$. In this same amount of time, the light wave travels $\lambda_0 + \lambda$ at speed c , which means that

$$\Delta t = \frac{\lambda_0}{v_z} = \frac{\lambda_0 + \lambda}{c}. \quad (2.6)$$

Also, it has been stated that $v = \beta c$, and

$$\boldsymbol{\beta} = (\beta_x, \beta_y, \beta_z), \quad (2.7)$$

from which

$$\beta^2 = \beta_x^2 + \beta_y^2 + \beta_z^2, \quad (2.8)$$

so

$$v_z = c\sqrt{\beta^2 - \beta_x^2 - \beta_y^2}, \quad (2.9)$$

or

$$v_z = c\sqrt{\beta^2 - \beta_\perp^2}, \quad (2.10)$$

where $\beta_\perp = \sqrt{\beta_x^2 + \beta_y^2}$ is the transverse velocity of the electron. It will be shown in the next section that the electrons' transverse velocity in the undulator is

$$\beta_\perp^2 = \frac{K^2}{\gamma^2}, \quad (2.11)$$

where the dimensionless undulator parameter is defined as $K \equiv eB\lambda_0/2\pi mc^2$, which is on the order of unity.

Therefore, equation (2.6) can be written as:

$$\frac{\lambda_0}{c\sqrt{\beta^2 - \beta_\perp^2}} = \frac{\lambda + \lambda_0}{c}, \quad (2.12)$$

and from equation (2.2), $\beta^2 = 1 - \gamma^{-2}$, so

$$\begin{aligned} \frac{\lambda_0}{\sqrt{\beta^2 - \beta_\perp^2}} &= \lambda + \lambda_0, \\ \frac{\lambda_0}{\sqrt{1 - \gamma^{-2} - \frac{K^2}{\gamma^2}}} &= \lambda + \lambda_0, \end{aligned}$$

and

$$\frac{\lambda_0}{\sqrt{1 - \frac{1 + K^2}{\gamma^2}}} = \lambda + \lambda_0. \quad (2.13)$$

Assuming $\gamma \gg 1$ and $K \approx 1$, then

$$\sqrt{1 - \frac{1 + K^2}{\gamma^2}} \approx 1 - \frac{1 + K^2}{2\gamma^2}. \quad (2.14)$$

Substituting the approximation from equation (2.14) into (2.13) yields

$$\lambda = \lambda_0 \frac{1 + K^2}{2\gamma^2}. \quad (2.15)$$

Equation (2.15) yields the wavelength of the light generated from the undulator at resonance. It is important to note that the wavelength depends upon the strength of the undulator magnetic field (which is incorporated in the dimensionless undulator parameter K), the undulator period, and the electron energy.

C. ELECTRON MOTION

Microscopic electron motion within the undulator and laser beam is governed by the pendulum equation. Another component of the relativistic Lorentz force equation is termed the energy equation, which is given as

$$\frac{d\gamma}{dt} = -\frac{e}{mc} \boldsymbol{\beta} \cdot \mathbf{E}, \quad (2.16)$$

and is an expression for the evolution of the electron energy over time within the undulator. [9]

Initially, it is assumed that there is no light in the cavity, so the relativistic Lorentz force equation is

$$\frac{d}{dt}(\gamma \boldsymbol{\beta}) = -\frac{e}{mc} (\boldsymbol{\beta} \times \mathbf{B}). \quad (2.17)$$

Now,

$$\boldsymbol{\beta} \times \mathbf{B} = B \begin{bmatrix} \hat{x} & \hat{y} & \hat{z} \\ \beta_x & \beta_y & \beta_z \\ \cos(k_0 z) & \sin(k_0 z) & 0 \end{bmatrix}, \quad (2.18)$$

so from equation (2.17) and (2.18) we have

$$\begin{aligned}
\frac{d}{dt}(\beta_x) &= \frac{eB\beta_z}{\gamma mc} \sin(k_0 z), \\
\beta_x &= -\frac{eB}{\gamma mc^2 k_0} \cos(k_0 z), \\
&= -\frac{eB\lambda_0}{2\pi\gamma mc^2} \cos(k_0 z), \\
\beta_x &= -\frac{K}{\gamma} \cos(k_0 z), \tag{2.19}
\end{aligned}$$

where $K=eB\lambda_0/2\pi mc^2$ again is the dimensionless undulator parameter, and the constant of integration is zero for perfect injection.

By a similar argument, it can be shown that

$$\beta_y = -\frac{K}{\gamma} \sin(k_0 z). \tag{2.20}$$

Combining these two equations yields

$$\boldsymbol{\beta}_\perp = -\frac{K}{\gamma} (\cos k_0 z, \sin k_0 z, 0). \tag{2.21}$$

This gives the velocity of the electrons perpendicular to the longitudinal direction. The magnitude of $\boldsymbol{\beta}_\perp$ is approximately 0.01, which shows that the perpendicular velocity of the electrons is much smaller than their velocity along the axis.

Assume that the longitudinal position of the electrons is given by $z(t) = \beta_z ct \approx ct$, so that $k_0 z \approx k_0 ct = \omega_0 t$. This means

$$\boldsymbol{\beta}_\perp = -\frac{K}{\gamma} (\cos \omega_0 t, \sin \omega_0 t, 0). \tag{2.22}$$

Integrating to get the electrons' transverse position yields

$$x_\perp = \frac{K}{\gamma} \frac{\lambda_0}{2\pi} (-\sin \omega_0 t, \cos \omega_0 t, 0), \tag{2.23}$$

where constants of integration are taken to be zero for perfect orbits. For a high power FEL, $K \approx 1$, $\gamma \approx 100$, and $\lambda_0 \approx 2.5$ cm, so that $x_\perp \approx 40\mu\text{m}$. The beam radius is typically $\approx 40\mu\text{m}$.

Now light will be incorporated to demonstrate its effect on the microscopic electron motion. The fields were given in equations (2.3) and (2.4). Inserting these into equation (2.1) yields

$$\frac{d}{dt}(\beta\gamma) = -\frac{e}{mc} \left[\underbrace{E(1-\beta_z)(\cos\psi, -\sin\psi, 0)}_{\text{optical field force}} + \underbrace{\beta_z B(-\sin k_0 z, \cos k_0 z, 0)}_{\text{undulator field force}} \right]. \quad (2.24)$$

Using equations (2.4), (2.16), and (2.21) we find

$$\dot{\gamma} = \frac{eKE}{\gamma mc} (\cos(k_0 z) \cos\psi - \sin(k_0 z) \sin\psi),$$

and

$$\dot{\gamma} = \frac{eKE}{\gamma mc} (\cos(k_0 z + \psi)) \quad (2.25)$$

where $\psi = kz - \omega t + \phi$. Defining $\zeta \equiv (k+k_0)z - \omega t$ as the electron phase shows that equation (2.25) can be rewritten as

$$\dot{\gamma} = \frac{eKE}{\gamma mc} \cos(\zeta + \phi). \quad (2.26)$$

In order for there to be an increase in the optical energy, the electrons must lose energy. Therefore, $\dot{\gamma}$ must be less than zero when averaged over all electrons in the beam.

In order to explore electron bunching, the electron phase ζ will be examined.

$$\begin{aligned} \zeta &= (k+k_0)z - \omega t, \\ \dot{\zeta} &= (k+k_0)\dot{z} - \omega, \\ \text{so that } \dot{\zeta} &= (k+k_0)\beta_z c - \omega. \end{aligned}$$

From equation (2.2), it can be shown that

$$\begin{aligned}
\gamma^{-2} &= 1 - \beta_{\perp}^2 - \beta_z^2, \\
&= 1 - \frac{K^2}{\gamma^2} - \beta_z^2, \\
\beta_z^2 &= 1 - \frac{1 + K^2}{\gamma^2}.
\end{aligned}$$

Using the approximation from equation (2.14),

$$\beta_z \approx 1 - \frac{1 + K^2}{2\gamma^2}. \quad (2.27)$$

Inserting this into the above equation for $\dot{\zeta}$ yields

$$\dot{\zeta} = (k + k_0) \left(1 - \frac{1 + K^2}{2\gamma^2} \right) c - \omega. \quad (2.28)$$

Since $\lambda \ll \lambda_0$, then $k \gg k_0$, so that k_0 is negligible compared to k . Making these approximations and differentiating equation (2.28) yields

$$\ddot{\zeta} = kc \left(\frac{1 + K^2}{\gamma^3} \right) \dot{\gamma}. \quad (2.29)$$

Substituting $\dot{\gamma}$ from equation (2.26) into the right-hand-side yields

$$\ddot{\zeta} = kc \left(\frac{1 + K^2}{\gamma^2} \right) \frac{eKE}{\gamma^2 mc} \cos(\zeta + \phi). \quad (2.30)$$

From equation (2.15) and the fact that $kc = \omega = 2\pi c/\lambda$, we find that

$$kc = \frac{2\pi c (2\gamma^2)}{\lambda_0 (1 + K^2)},$$

or

$$kc = k_0 c \left(\frac{2\gamma^2}{1 + K^2} \right). \quad (2.31)$$

Substituting this into equation (2.30) yields

$$\ddot{\zeta} = \frac{2k_0 eEK}{\gamma^2 m} \cos(\zeta + \phi). \quad (2.32)$$

The concept of dimensionless time is introduced to further clarify equation (2.32). Let $\tau \equiv ct/L$, where L is the overall length of the undulator, so that $\tau = 0$ corresponds to the entrance of the undulator and $\tau = 1$ the exit. Therefore,

$$d\tau = \frac{c}{L} dt,$$

$$\frac{d^2}{d\tau^2} \zeta = \frac{d^2}{dt^2} \zeta \left(\frac{L}{c} \right)^2,$$

so

$$\zeta^{\circ\circ} = \frac{2eEK L^2 k_0}{\gamma^2 m c^2} \cos(\zeta + \phi). \quad (2.33)$$

Here $\frac{d^2}{d^2\tau}(\dots)$ symbolizes $\frac{d^2}{d^2\tau}(\dots)$, the second dimensionless time derivative. Now

$$L = N\lambda_0 = \frac{2\pi N}{k_0},$$

or $Lk_0 = 2\pi N$.

Inserting this into equation (2.33) yields

$$\zeta^{\circ\circ} = \frac{4\pi NeKLE}{\gamma^2 m c^2} \cos(\zeta + \phi). \quad (2.34)$$

Defining the optical field amplitude as

$$|a| \equiv \frac{4\pi NeKL}{\gamma^2 m c^2} E \quad (2.35)$$

allows equation (2.34) to be written as

$$\zeta^{\circ\circ} = |a| \cos(\zeta + \phi). \quad (2.36)$$

This demonstrates that the electron's phase behavior within the undulator is governed by the pendulum equation, driven by the optical field of amplitude $|a|$. The dimensionless phase velocity of the electron is then defined as

$$\nu = \dot{\zeta} = L[(k + k_0)\beta_z - k] \quad (2.37)$$

Equations (2.36) and (2.37) are significant because they facilitate the modeling of the microscopic electron motion within the undulator, which will be explored in a later section.

D. THE OPTICAL WAVE EQUATION

The final step in describing the theory behind the Free Electron Laser is to analyze the interaction between the electrons and the optical wave they create. The optical wave equation is

$$\left(\nabla^2 - \frac{1}{c^2} \frac{\partial^2}{\partial t^2} \right) \mathbf{A}(\mathbf{x}, t) \approx -\frac{4\pi}{c} \mathbf{J}_\perp(\mathbf{x}, t), \quad (2.38)$$

in which the vector potential, \mathbf{A} , for a helical undulator is given by

$$\mathbf{A} = \frac{E}{k} (\sin \psi, \cos \psi, 0), \quad (2.39)$$

where $\psi = kz - \omega t + \phi$, from which

$$\mathbf{B}_s = \bar{\nabla} \times \mathbf{A} \quad (2.40)$$

and

$$\mathbf{E}_s = -\frac{1}{c} \frac{\partial \mathbf{A}}{\partial t} \quad (2.41)$$

yields the specified field \mathbf{B}_s and \mathbf{E}_s , and \mathbf{J}_\perp is the transverse current density.

In order to solve this equation, a number of assumptions will be made. First, the optical waves are assumed to be plane waves, so that there is no change in the perpendicular components of \mathbf{A} , and only the longitudinal components of the Laplacian survive. This means that

$$\nabla^2 \mathbf{A} \approx \frac{\partial^2}{\partial z^2} \mathbf{A} \quad (2.42)$$

The second assumption is that the fields are slowly varying in z and t . This means that, in the time domain, during an optical period $\dot{E} \ll \omega E$ and $\dot{\phi} \ll \omega \phi$, and in space, over an optical wavelength $E' \ll kE$ and $\phi' \ll k\phi$. [3 p.13] This allows all second-order and

higher terms to be neglected. When equation (2.39) is substituted into (2.38), these assumptions simplify the expression to

$$2\left(\frac{\partial E}{\partial z} + \frac{1}{c}\frac{\partial E}{\partial t}\right)(\cos\psi, -\sin\psi, 0) - 2E\left(\frac{\partial\phi}{\partial z} + \frac{1}{c}\frac{\partial\phi}{\partial t}\right)(\sin\psi, \cos\psi, 0) \approx -\frac{4\pi}{c}\mathbf{J}_\perp. \quad (2.43)$$

In order to express equation (2.43) in dimensionless parameters, the spatial and time derivatives can be expressed in terms of the undulator length L and dimensionless time τ . The spatial coordinate z^* is used to define a point that follows the light and is defined as

$$z^* = z - ct. \quad (2.44)$$

From the definition of $\tau = ct/L$, equation (2.44) can be rewritten as

$$z^* = z - L\tau \quad (2.45)$$

This allows the partial derivatives to be written as

$$\frac{\partial}{\partial z} = \frac{\partial z^*}{\partial z} \frac{\partial}{\partial z^*} + \frac{\partial \tau}{\partial z} \frac{\partial}{\partial \tau} \quad (2.46)$$

and

$$\frac{\partial}{\partial t} = \frac{\partial z^*}{\partial t} \frac{\partial}{\partial z^*} + \frac{\partial \tau}{\partial t} \frac{\partial}{\partial \tau}. \quad (2.47)$$

Using the definition of τ and equation (2.45), $\partial z^* / \partial z = 1$, $\partial z^* / \partial t = -c$, $\partial \tau / \partial z = 0$, and $\partial \tau / \partial t = c/L$. Equations (2.46) and (2.47) then become

$$\frac{\partial}{\partial z} = \frac{\partial}{\partial z^*} \quad (2.48)$$

and

$$\frac{\partial}{\partial t} = -c \frac{\partial}{\partial z^*} + \frac{c}{L} \frac{\partial}{\partial \tau}. \quad (2.49)$$

Combining equations (2.48) and (2.49) yields the operator

$$\frac{\partial}{\partial z} + \frac{1}{c} \frac{\partial}{\partial t} = \frac{\partial}{\partial z^*} + \frac{1}{c} \left[-c \frac{\partial}{\partial z^*} + \frac{c}{L} \frac{\partial}{\partial \tau} \right] = \frac{1}{L} \frac{\partial}{\partial \tau} \quad (2.50)$$

When this operator is applied to equation (2.43), it is then written as

$$\frac{2}{L} \frac{\partial E}{\partial \tau} (\cos \psi, -\sin \psi, 0) - \frac{2E}{L} \frac{\partial \phi}{\partial \tau} (\sin \psi, \cos \psi, 0) \approx -\frac{4\pi}{c} \mathbf{J}_\perp. \quad (2.51)$$

In order to solve this equation, the vector components must be decoupled. This is done by defining two unit vectors, $\hat{\epsilon}_1 = (\cos \psi, -\sin \psi, 0)$ and $\hat{\epsilon}_2 = (-\sin \psi, -\cos \psi, 0)$. Multiplying equation (2.51) by these two unit vectors individually yields

$$\frac{\partial E}{\partial t} = -\frac{2\pi L}{c} \mathbf{J}_\perp \cdot \hat{\epsilon}_1 \quad (2.52)$$

and

$$E \frac{\partial \phi}{\partial t} = -\frac{2\pi L}{c} \mathbf{J}_\perp \cdot \hat{\epsilon}_2. \quad (2.53)$$

The transverse current density \mathbf{J}_\perp is generated by the transverse motion of the electron within the undulator, and is the sum of the individual electron currents, given by

$$\mathbf{J}_\perp = \sum_i \left[-ec \boldsymbol{\beta}_\perp \delta^3(\mathbf{x} - \mathbf{r}_i) \right], \quad (2.54)$$

where $\delta^3(\mathbf{x} - \mathbf{r}_i)$ is the three dimensional Dirac delta function and \mathbf{r}_i is the position of the i^{th} electron. Inserting this expression, as well as $\boldsymbol{\beta}_\perp$ from equation (2.21), yields

$$\frac{\partial E}{\partial t} = -\frac{2\pi KeL}{\gamma} \sum_i \delta^3(\mathbf{x} - \mathbf{r}_i) (\cos(k_0 z) \cos \psi - \sin(k_0 z) \sin \psi) \quad (2.55)$$

and

$$E \frac{\partial \phi}{\partial \tau} = \frac{2\pi KeL}{\gamma} \sum_i \delta^3(\mathbf{x} - \mathbf{r}_i) (\cos(k_0 z) \sin \psi - \sin(k_0 z) \cos \psi). \quad (2.56)$$

The above summation of electron phases can be replaced by the volume density ρ_e of electrons and an average over sampled electrons $\langle \dots \rangle$. This, along with trigonometric identities and the definition $\zeta = (k + k_0)z - \omega t$ given in section 2.C yields

$$\frac{\partial E}{\partial \tau} = -\frac{2\pi KeL \rho_e}{\gamma} \langle \cos(\zeta + \phi) \rangle \quad (2.57)$$

and

$$E \frac{\partial \phi}{\partial \tau} = \frac{2\pi KeL\rho_e}{\gamma} \langle \sin(\zeta + \phi) \rangle, \quad (2.58)$$

where $\langle \dots \rangle$ is the average over all sampled electrons. Multiplying equation (2.58) by i and adding it to (2.57) recombines the separated equations, and yields

$$\frac{\partial E}{\partial \tau} + iE \frac{\partial \phi}{\partial \tau} = -\frac{2\pi KeL\rho_e}{\gamma} \langle e^{-i(\zeta + \phi)} \rangle. \quad (2.59)$$

Multiplying both sides of the equation by $e^{i\phi}$ allows it to be written as

$$\frac{\partial}{\partial \tau} (E e^{i\phi}) = -\frac{2\pi KeL\rho_e}{\gamma} \langle e^{-i\zeta} \rangle. \quad (2.60)$$

Equation (2.35) can be written as

$$\frac{|a| \gamma^2 m c^2}{4\pi NeKEL} = 1, \quad (2.61)$$

so the left side of equation (2.60) can be multiplied by (2.61) without loss of equality, and can therefore be written as

$$\frac{\partial a}{\partial \tau} = \overset{\circ}{a} = -j \langle e^{-i\zeta} \rangle, \quad (2.62)$$

where $a = |a| e^{i\phi}$ is the complex dimensionless optical field and j is defined as the dimensionless current density, which is

$$j = \frac{8\pi^2 K^2 e^2 L^2 \rho_e N}{\gamma^3 m c^2}. \quad (2.63)$$

Equation (2.62) demonstrates that the evolution of the optical field is dependent upon the electron beam current and the average phase of the electrons.

E. GAIN

Gain, G , is defined as the fractional change of power in the optical field per pass through the undulator, and is given by

$$G = \frac{a_1^2 - a_0^2}{a_0^2} \quad (2.64)$$

where a_0 and a_1 are the dimensionless optical field strengths at $\tau = 0$ and $\tau = 1$, i.e. the beginning and end of the undulator, respectively. In each pass through the undulator, energy is transferred between the electrons and the optical field. Therefore, the gain can be analyzed by determining the change in the energy of the electrons.

It will first be shown that a change in the electron energy is proportional to its change in phase velocity. This phase velocity v was given in equation (2.37) as

$$v = L \left[(k + k_0) \beta_z - k \right]. \quad (2.65)$$

Because $k_0 \ll k$ for relativistic electrons, this can be written as

$$\Delta v \approx L k \Delta \beta_z \quad (2.66)$$

Using $k = 2\pi / \lambda$ and the resonance condition defined in equation (2.15), with $N = L / \lambda_0$, this can be written as

$$\Delta v \approx 2\pi N \left(\frac{2\gamma^2}{1 + K^2} \right) \Delta \beta_z. \quad (2.67)$$

In section 2.C, it was shown that

$$\beta_z^2 = 1 - \frac{1 + K^2}{\gamma^2}. \quad (2.68)$$

Taking the time derivative of both sides and solving for $\dot{\beta}_z$ yields

$$\dot{\beta}_z = \frac{\dot{\gamma}}{\gamma^3} \frac{1 + K^2}{\beta_z}. \quad (2.69)$$

Multiplying both sides by Δt and using $\Delta \beta_z = \dot{\beta}_z \Delta t$ and $\Delta \gamma_z = \dot{\gamma}_z \Delta t$ yields

$$\Delta \beta_z = \frac{\Delta \gamma (1 + K^2)}{\gamma^3 \beta_z} \quad (2.70)$$

Using the approximation that $\beta_z \approx 1$, equation (2.70) is inserted into equation (2.67) to yield the relationship between Δv and $\Delta \gamma$, which is

$$\Delta v = 4\pi N \frac{\Delta \gamma}{\gamma}. \quad (2.71)$$

Solving for $\Delta\gamma$ and multiplying both sides of the resulting equation by mc^2 yields

$$(\Delta\gamma)mc^2 \approx \frac{\gamma mc^2}{4\pi N} (\langle v \rangle - v_0) \quad (2.72)$$

where $\langle v \rangle$ is the average electron phase velocity for all electrons at the end of the undulator and v_0 is the initial electron phase velocity. Since γmc^2 is the energy of the electrons, this equation shows the change in an individual electron's energy in terms of the change in electron phase velocity. The number of electrons within a small a length dV in an optical wave is $dN_e = \rho F dV$ where F is the filling factor, defined as the cross-sectional area of the electron beam divided by the cross-sectional area of the optical beam. The initial energy of the volume element of the optical beam is

$$dE_0 = \frac{E^2}{4\pi} dV, \quad (2.73)$$

for circularly polarized light. The gain is calculated assuming the lost energy of the electron beam is converted to laser energy, so that

$$G = \frac{\Delta E_{\text{electron-beam}}}{dE_{\text{optical-beam}}} = - \frac{\rho F dV \frac{\gamma mc^2 (\langle v \rangle - v_0)}{4\pi N}}{\frac{E^2}{4\pi} dV} \quad (2.74)$$

$$G = - \frac{\rho F \gamma mc^2 (\langle v \rangle - v_0)}{NE^2}. \quad (2.75)$$

From equations (2.35) and (2.63)

$$\frac{j}{a_0^2} = \frac{\gamma \rho mc^2}{2NE^2}. \quad (2.76)$$

Substituting this into equation (2.75) allows the gain equation to be written as

$$G = - \frac{2jF}{a_0^2} (\langle v \rangle - v_0). \quad (2.77)$$

This equation shows that in order for there to be positive gain, the average phase velocity must be less than the initial electron phase velocity. Therefore, there has to be a net loss of electron phase velocity in order to achieve positive gain in a FEL.

F. PHASE SPACE

Phase space is a useful graphical technique for understanding the physics of the pendulum equation. As was shown in section 2.C, electron motion within the undulator is governed by the pendulum equation (equation (2.36)), so the use of phase space is an ideal method to show the evolution of the electrons. The electrons' phase ζ and phase velocity $v = \dot{\zeta}$ are plotted on the horizontal and vertical axes, respectively, as in Figure 4 below, over one pass through the undulator.

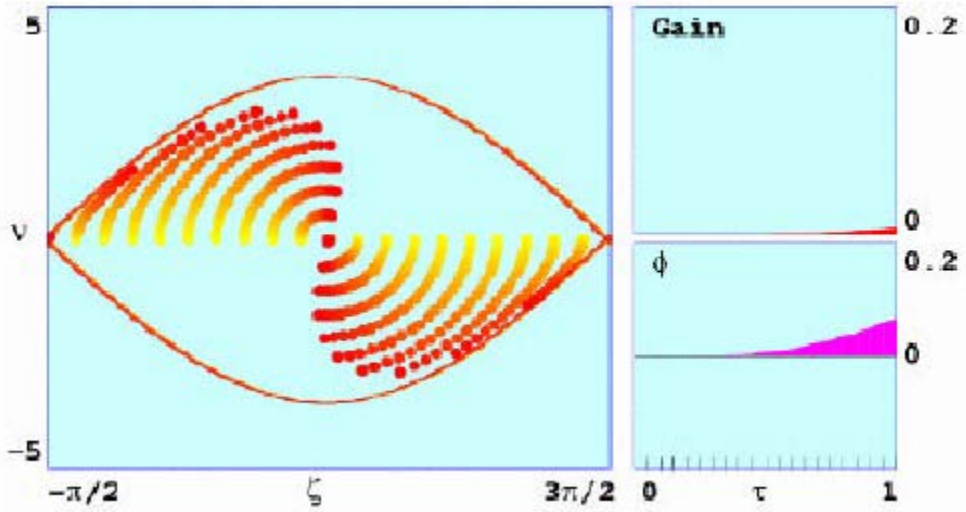


Figure 4. Phase Space Plot for Electrons on Resonance

The width of the window is a section of the electron beam one wavelength of light long, and moves along at the speed of an electron at resonance. In Figure 4, 20 sample electrons are followed from $\tau = 0$ to $\tau = 1$, symbolized by the change of the color of the tracks from yellow to red, respectively. Because the electrons' energy change is proportional to v , this plot demonstrates the evolution of the electrons' energy as well. In this case, all electrons start at an initial phase velocity of $v_0 = 0$, or at resonance, and are uniformly distributed from $-\pi/2 < \zeta < 3\pi/2$. It can be seen in Figure 4 that while the electrons that begin below $\zeta = 0$ gain energy, those greater than $\zeta = 0$ lose the same amount. This means that there is no net transfer of energy from the electrons to the optical field.

The red line around the electrons is the separatrix, which shows the demarcation between open and closed orbits. The electrons that start outside this line will have open orbits, while those that are contained within it follow closed orbits.

In Figure 5 below, the electrons are injected with an initial phase velocity $v_0 = 2.6$, again uniformly distributed along ζ .

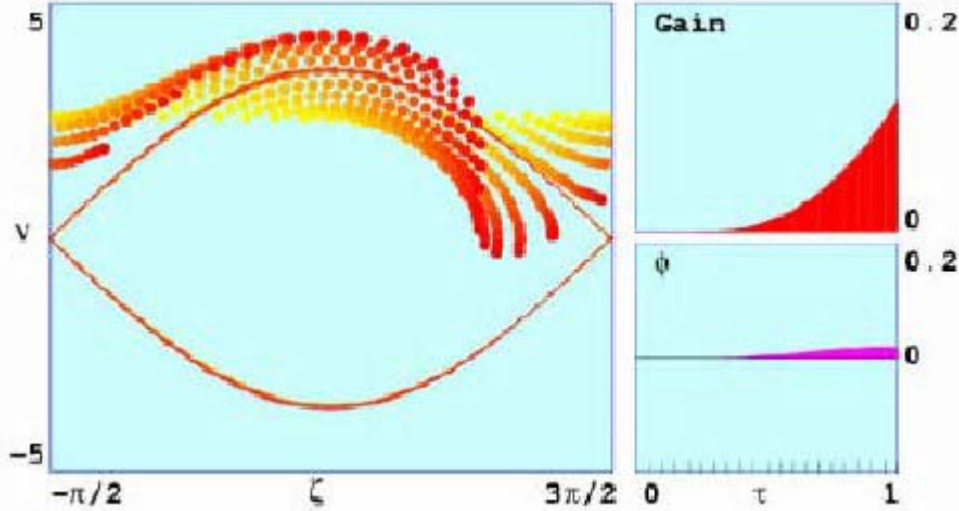


Figure 5. Phase Space Plot With $v_0=2.6$.

Note that in Figure 5, more electrons lose energy than gain energy. This net loss of electron energy means that there is gain in the optical field. This gain is graphed in the upper right hand side of the figure.

Figures 4 and 5 are idealized examples of simulation outputs. Real electrons will not all arrive at the undulator with the same v_0 , so electrons within simulations are given an initial energy spread in order to accommodate this practical issue. The use of sample electrons increases the speed of simulations, but may decrease accuracy. Therefore many more sample electrons than the 20 shown in the above figures are used. Simulations conducted in order to optimize FEL performance use this and other techniques to demonstrate the output that can be achieved for a given set of parameters. This will be further explored in later sections.

THIS PAGE INTENTIONALLY LEFT BLANK

III. MULTIPLE BEAM DIRECTORS

The theory which describes a megawatt-class free electron laser is essentially the same as that for existing FELs. Ongoing engineering improvements optics and cathodes indicate that megawatt operation can be realized in the future.

However, one thing that will limit all weapons-grade lasers is thermal blooming. Thermal blooming is caused by heating of the atmosphere as a result of absorption of laser beam energy traveling through a volume of air. Because the optical beam has a Gaussian cross section, with its peak in the center, the heating is more significant in the center of the beam than the outer edges. The resulting gradient in the refractive index of the air through which it is passing causes the light to bend away from the warmer center of the beam, and thus behave as if it were going through a diverging lens. This defocusing can greatly degrade laser effectiveness.

As has already been mentioned, the free electron laser possesses the important attribute of tunability. This is important because there have been numerous studies that investigate which wavelengths of light pass through the atmosphere with the least absorption. Figure 6 below shows the percent transmission for light of various wavelengths. It also shows at which wavelengths absorption by CO_2 and H_2O molecules is most significant.

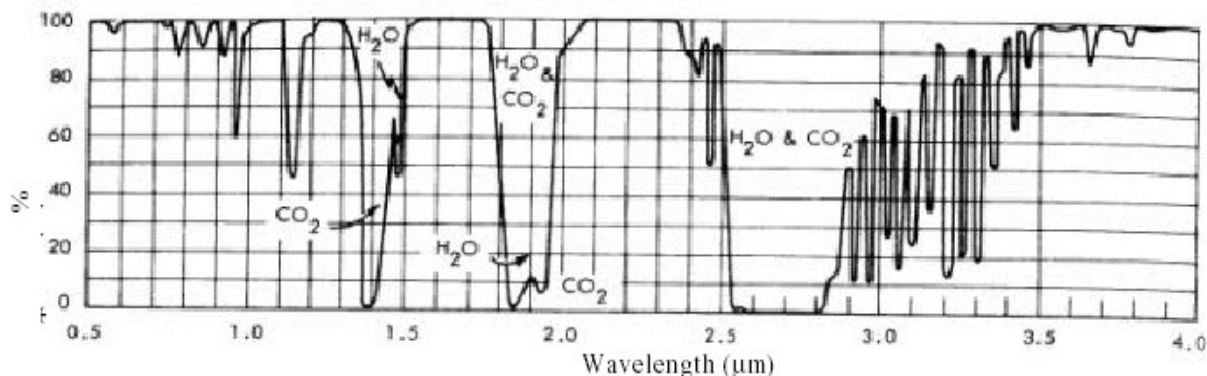


Figure 6. Transmittance of 1000 ft horizontal path at sea level at 79°F containing 5.7mm precipitable water [13]

Because of tunability, the FEL can produce light at the best wavelength for maritime applications, which has been determined to be approximately 1 μm . Despite this advantage, thermal blooming is still a significant problem. One way to combat this is the use of multiple beam directors, which is the topic of this chapter.

A. DISCUSSION

There are numerous advantages to using multiple beam directors. By sending a fraction of the total energy through each volume of space, the heating of the atmosphere is reduced. Therefore, thermal blooming can occur far enough along in the beam path as to have little to no impact, which is the topic of the next section. This can allow for greater power on target because these beams can be aimed such that they are focused on the same spot. While less energy passes through each volume of air, the total energy desired is still focused to one spot at the target.

Rather than combining the beams at the target, another possibility is to focus each director on a different section of the target. For targets of sufficient size, directors could be focused on different sections in order to gain the advantages of each aim point. For example, one could be focused on the nose cone in order to destroy the aerodynamics, guidance systems, and other components contained within, while the other focuses on a flight control surface such as a wing to destroy the stability and control. This would increase the dwell time required, but may be a viable option for lower velocity targets. Another option for targets that allow a longer dwell time is the ability to make the affected area bigger. Instead of focusing the beams on the same spot, they can be focused adjacent to each other, doubling the affected area.

One drawback of this may be the additional space required on the ship. Directors are large and complicated, as can be seen in a conceptual drawing, Figure 7 below.

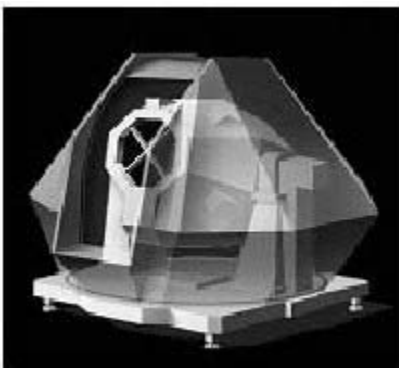


Figure 7. Conceptual laser beam director.

This complication has already been addressed, however. In most proposals for laser placement on ships, two directors are required in order to ensure 360° coverage. Figure 8 below shows one such proposal for fore-and-aft mounted directors. The left picture shows a close-up view of the firing arcs, while the right is expanded to show the overlap areas where two beams can hit the same target. This shows that the angular coverage of which two directors are capable is approximately 80° on each side, allowing for the beams to be able combine on a single target for almost half of the total coverage area. This is by no means the only configuration that can be used in order to achieve 360° coverage, but it is the most common. Because two beam directors will most likely be placed on the ship for this reason, it makes sense to develop the necessary techniques in order to direct both beams to a single target in any direction. The advantages of different placement options will be explored in a later section.

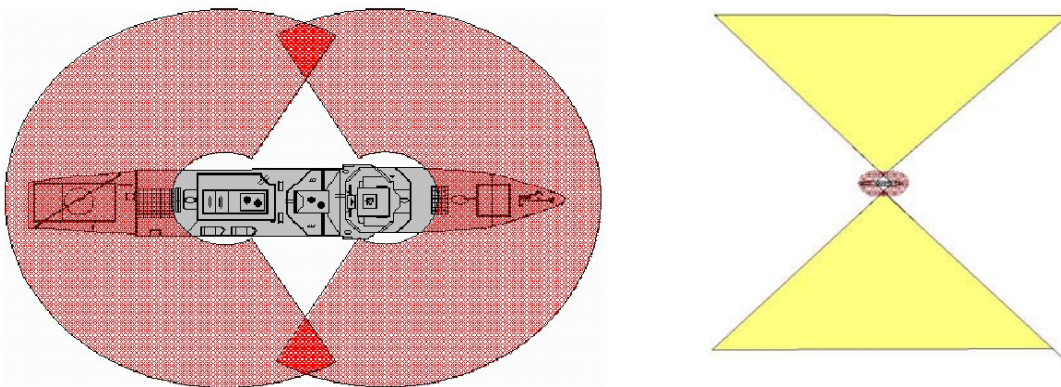


Figure 8. Firing arcs for directors placed fore and aft.

B. EFFECT OF DISTANCE ALONG BEAM OF THERMAL BLOOMING

1. Simulation Methods

As was mentioned above, the most significant way that using multiple beam directors will help decrease thermal blooming is the fact that the point where it takes place, called the stagnation zone, is moved to near the end of the beam's path. This allows less time for the beam to diffract, so the spot size is not increased as much as it would be if thermal blooming took effect earlier in the beam.

In order to study this, computer models of the beam path were used to demonstrate the effect of moving the stagnation zone. This simulation method is shown below from [5].

The parabolic wave equation describes the propagation of a laser beam to a target:

$$\frac{\partial}{\partial \tau_r} = \frac{i}{4} \nabla_{\perp}^2 a, \quad (3.1)$$

where the complex field $a = |a|e^{i\phi}$ evolves in dimensionless time $\tau_r = 0 \rightarrow 1$ along the range to target, and $\nabla_{\perp}^2 = \partial_x^2 + \partial_y^2$ is the dimensionless transverse Laplacian. Equation (3.1) uses the dimensionless field amplitude $|a|$, which is proportional to the actual optical field amplitude $|E|$, as derived in Chapter II. The initial Gaussian field shape at $\tau_r = 0$ is given by $a(r) = a_0 e^{-r^2/w^2} e^{i\phi} / w$, where $\phi = -r^2 \tau_w / (z_0^2 + \tau_w^2)$, $r^2 = x^2 + y^2$, $a_0 = 1$, and $w^2 = 1 + \tau_w^2 / z_0^2$, for a dimensionless Rayleigh length z_0 and beam waist at τ_w .

The result of the simulation yields a matrix of optical amplitudes, which are then plotted. Figure 9 below shows the side and end-on views of a beam traveling through the atmosphere with no blooming effects.

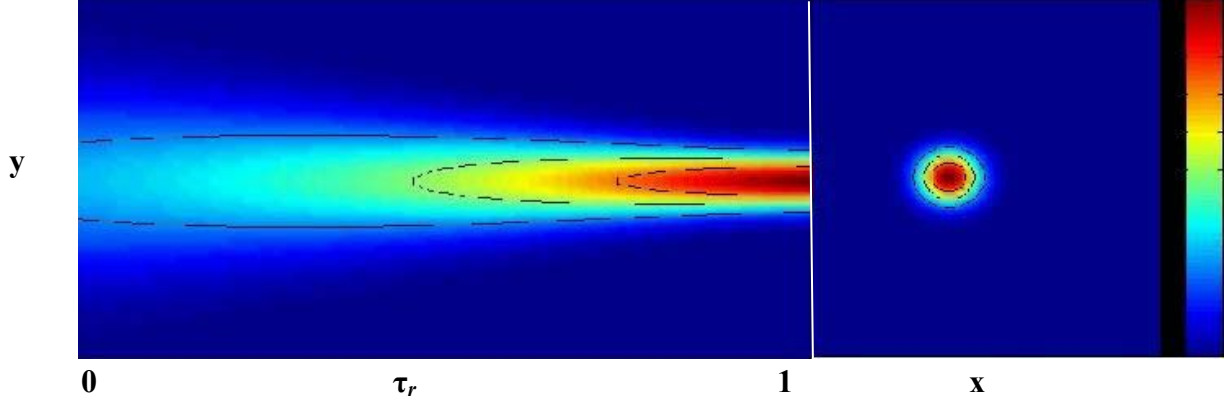


Figure 9. Beam propagation with no thermal blooming.

The color scale on the right of the figure shows the amplitude of the optical field, blue being the lowest and red the highest. The left side of the figure shows a side view of the beam as it travels from a source on the left ($\tau_r = 0$) to target on the right ($\tau_r = 1$). It is expanded for the purposes of illustration, as the actual beam diameter tapers from a meter to five centimeters, and the distance is on the order of eight kilometers. The right side is an end-on view of the beam at full range. Notice the clearly defined, concentric circles of intensity. This is due to the Gaussian intensity profile mentioned in the introduction of this section. The area of this circle is the focus of this analysis.

The stagnation zone is modeled by inserting a phase distortion into the path of the beam,

$$a_{out}(x, y) = e^{-i|a(x, y)|^2 d\phi_s} a_{in}(x, y) \quad (3.2)$$

where $d\phi_s$ is the effective zone strength of the lens.

2. Simulation Results

The next figure shows, from top to bottom the effect of placing a stagnation zone at distances of 30%, 50%, and 80% ($\tau_r = 0.3, 0.5$, and 0.80 , respectively) along the beam path.

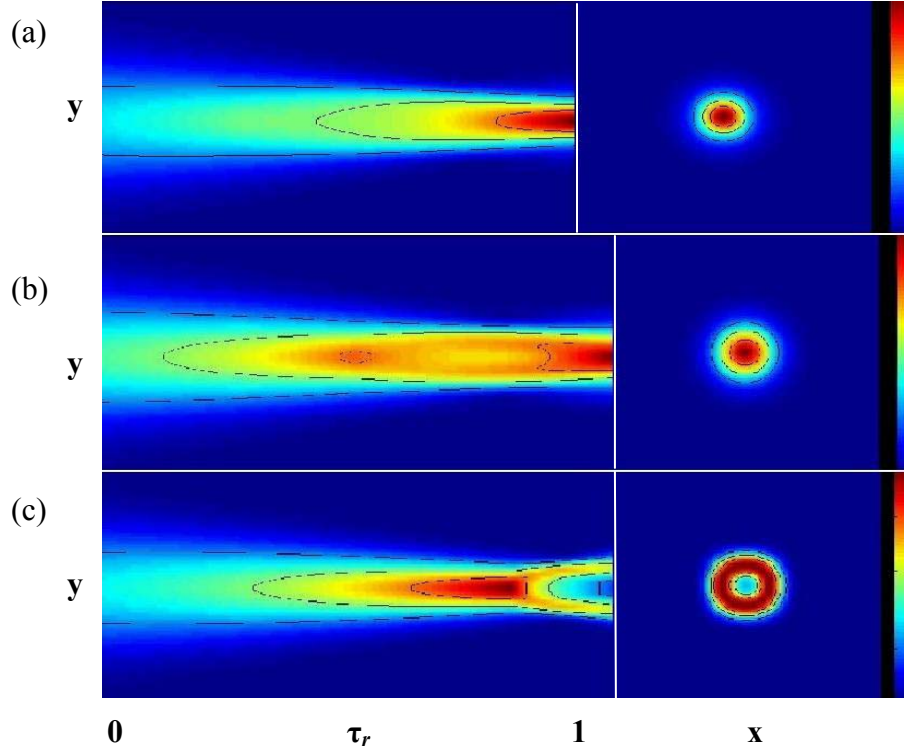


Figure 10. Stagnation zone at (a) 30%, (b) 50% and (c) 80% of total range.

Notice the diffraction of the beam and the increased size of the spot on the right side of the figures. The total area decreases as the zone is moved further along the beam.

The strength of the stagnation zone in the model can be varied as well as the location. In Figure 11 below, the area of the spot is plotted as a function of the distance along the beam for various zone strengths. The vertical axis is normalized to the radius of a spot that is unaffected by thermal blooming, where A is the area of the affected spot, and A_0 the area of the unaffected spot. The horizontal axis is τ_c , the location along the dimensionless path where the stagnation zone is located. The strength of the zone is noted in the legend, which is the value of $d\phi_s$ from equation (3.2).

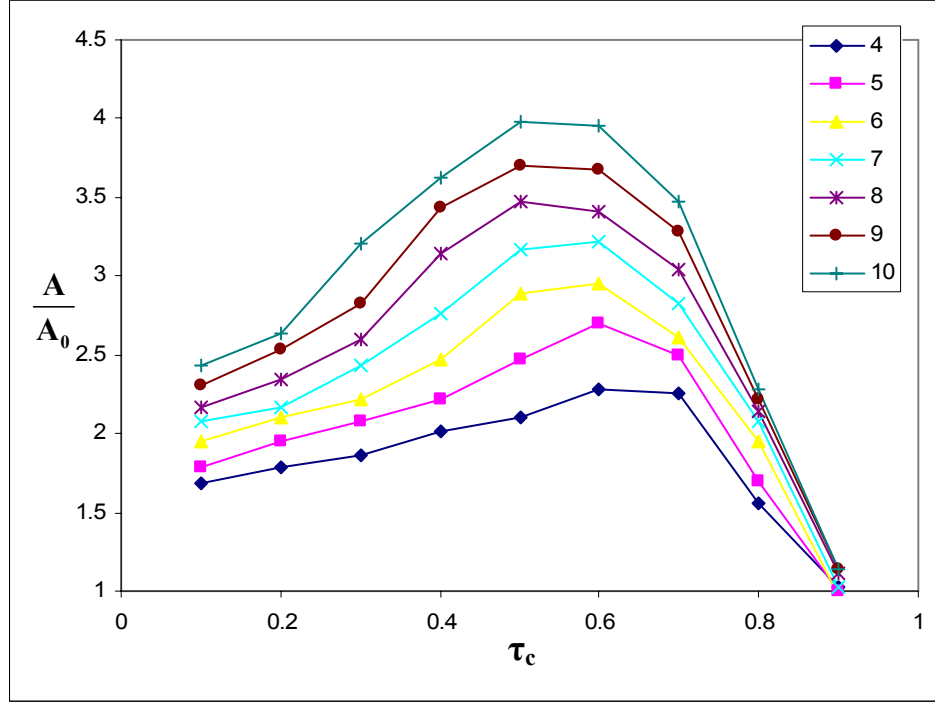


Figure 11. Positioning of the stagnation zone for varying strength of the zone.

The area of the spot for beams affected by blooming is much larger than the area of a spot from an unaffected beam. It reaches a maximum when blooming occurs at approximately 55% of the range to target, and then drops sharply after. An interesting feature of this plot is the aforementioned peak. This is due to the area of the beam at the time blooming takes effect. Near the source of the beam at the ship, the beam has a relatively large area, and therefore the intensity is lower so blooming tends not to occur. As can be seen in equation (3.2), the strength of the stagnation zone is dependent on the amplitude of the optical field, so the lens effect is weaker than it is later in the beam. The fall off of the area following the maximum is due to the lack of distance after blooming occurs for the beam to expand. Even though the blooming is stronger, as the stagnation zone moves toward the target, the beam has less time to expand, so the spot size decreases as the zone approaches the termination of the beam. These effects can also be seen in Figure 10.

Figure 12 shows a more complete three dimensional plot of the effect of the strength and position of the stagnation zone.

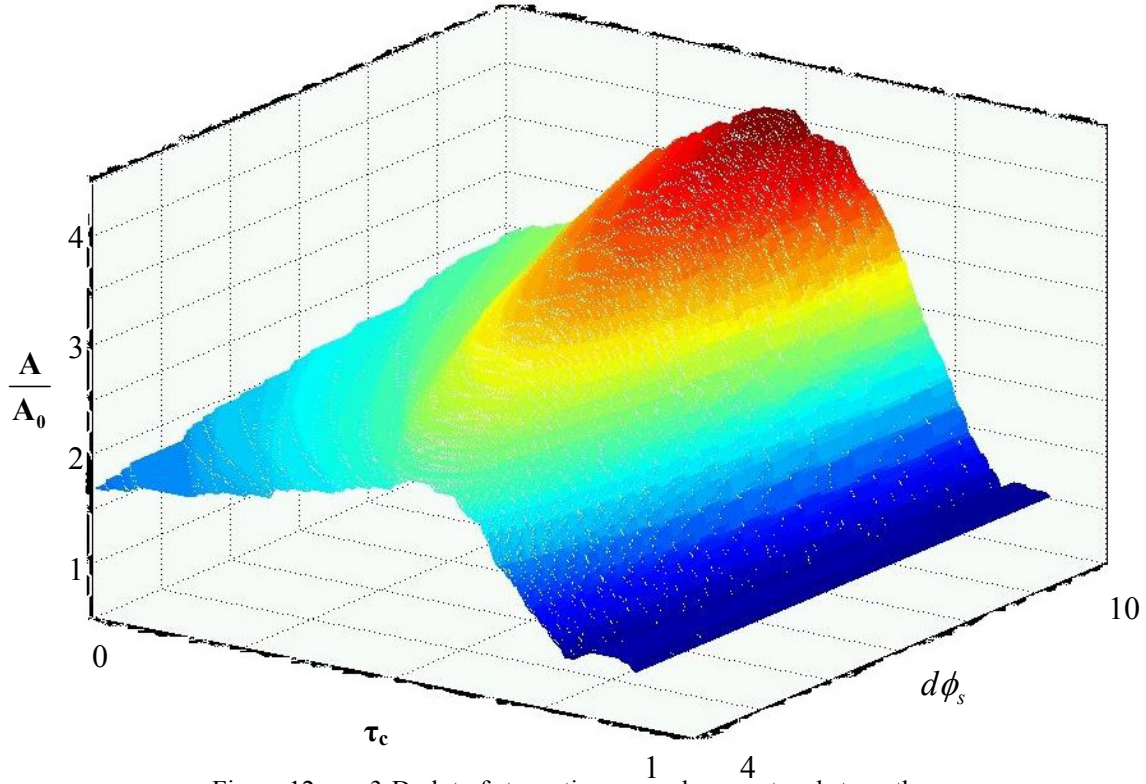


Figure 12. 3-D plot of stagnation zone placement and strength.

Both figures shows the advantage of moving the stagnation zone to as close to the target as possible. The spot size is close to that of an unaffected beam when the location of the stagnation zone is $>90\%$ of the distance to the target. As will be shown later, the use of multiple beams causes the stagnation zone, if it does occur, to be located at $>99\%$ of the distance to the target, so that the area will be barely affected by blooming.

C. GEOMETRIC DERIVATION OF BEAM OVERLAP

In order to determine the advantages of multiple beam directors, it is necessary to investigate the amount of overlap that the two beams will experience in their path to the target. This will allow for determining how much the atmosphere will be heated, and therefore the degree to which the probability of thermal blooming will be lessened.

This section of the thesis will show how the amount of overlap the beams will experience is determined as a function of their distance apart from each other on the ship. For the purposes of this analysis, the beams will be assumed to be firing at a spot that is equidistant between the two directors. For example, directors placed fore-and-aft will be firing at a target approaching directly perpendicular to the middle of the ship.

A simple geometric derivation will show how this is done. Figure 13 below shows the termination of the beams, where they overlap in which r_t is the radius of the beam at the target, l_0 is the length of the overlap, l_p is the length before the overlap, l_t is the distance to the target, x_s is the distance off-axis of the directors, and r_s is the radius of the directors (source).

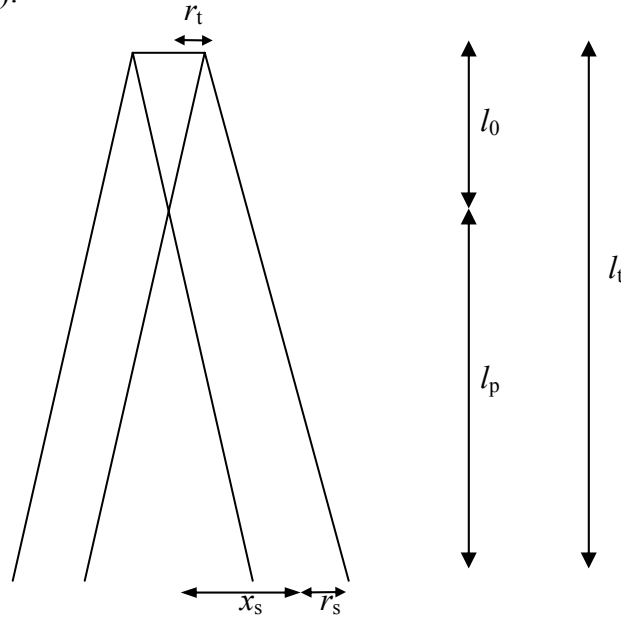


Figure 13. Overlap of beams at target

In order to determine the percent of the range that the beams are overlapping, look at one side of this figure.

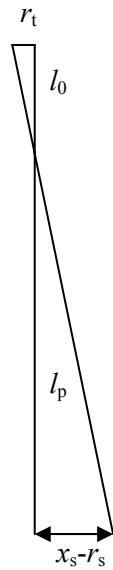


Figure 14. Triangular representation of beam overlap

Similar triangles yield that

$$\frac{r_t}{x_s - r_s} = \frac{l_0}{l_p}. \quad (3.3)$$

The desired radius of the beam at the target, r_t , is about 5 cm, and the radius of the director is approximately 0.5 m. Therefore, given a distance between the directors, $2x_s$, a ratio is found using equation 3.1 that gives the percentage of the range over which the beams are overlapping, which will be analyzed in the next section. It is worth noting that this range gives the initial point where the beams start touching each other. This means that the power is not automatically double at this point. Only at the actual aim point are the beams fully overlapping, and doubled in power.

In order to calculate the volume that is contained within the overlapping beams, make the simplifying assumption that they are rectangular solids. The volume is

$$V = \frac{1}{2}(2r_t)l_p h \quad (3.4)$$

where h is the height of the beams, as in Figure 15 below. The height h is assumed to be constant, and is estimated to be 10 cm, consistent with the above assumption of a 5 cm radius spot size.

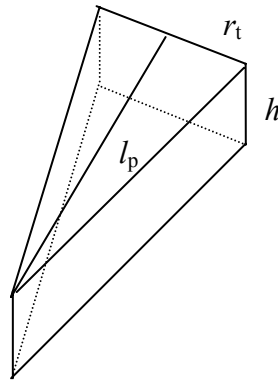


Figure 15. Overlapping volume.

D. PLACEMENT OPTIONS FOR TWO DIRECTORS

As has been mentioned, there are numerous options for the placement of multiple directors. The advantage of the fore-and-aft placement is 360° coverage, but this may

also be accomplished by placing them amidships on the port and starboard sides. Or they could be placed on the forward superstructure to one side, and aft on the other. These types of configurations would allow 360° coverage, but do not allow for overlap, so these are not ideal cases for this proposal. Therefore, discussion will be focused on fore-and-aft placement, with some consideration given to tandem-mounted directors.

Figure 16 below shows the overlap length of the beams as a function of the horizontal separation of the beam directors. This is given as the percentage of the total range to the target that the beams initially touch.

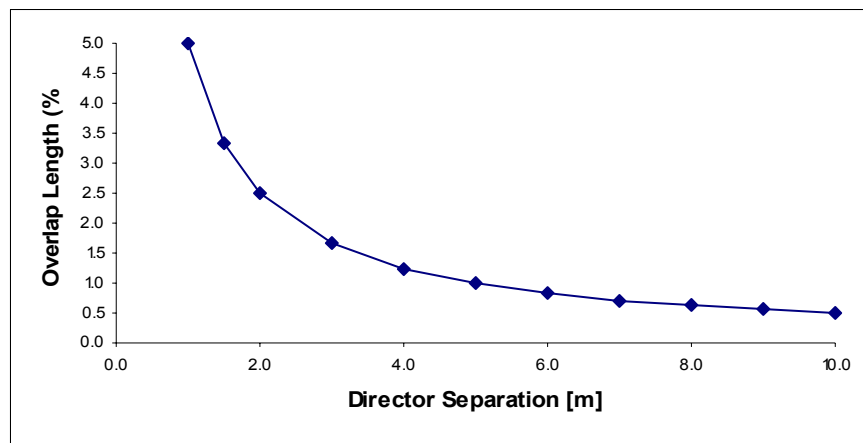


Figure 16. Percent overlap of two beam directors.

This shows that the percent of the overlap decreases quickly as the directors are separated. Fore-and-aft placement would extend the axis to much larger values. The typical length for a cruiser or destroyer is approximately 155 m. If the directors were at this separation, the overlap length would be only 0.03%. The length of an aircraft carrier is approximately 335 m, which yields 0.015%. For a range of 8 km, this yields a distance from initial contact of the two beams to termination at the target of only 2.6 m and 1.2 m, respectively.

If it were determined that placing two directors on one mount was a desirable alternative in order to take advantage of multiple beams, then they could conceivably be placed approximately 2 m apart. From the above graph, this yields 2.5%, which means an overlap distance of only 200 m at 8 km range.

Using the geometrical derivation in section 3.B, an approximate volume of the overlapping sections can be determined. This discussion will look at the 155m and 335m separation as shown in the following graph.

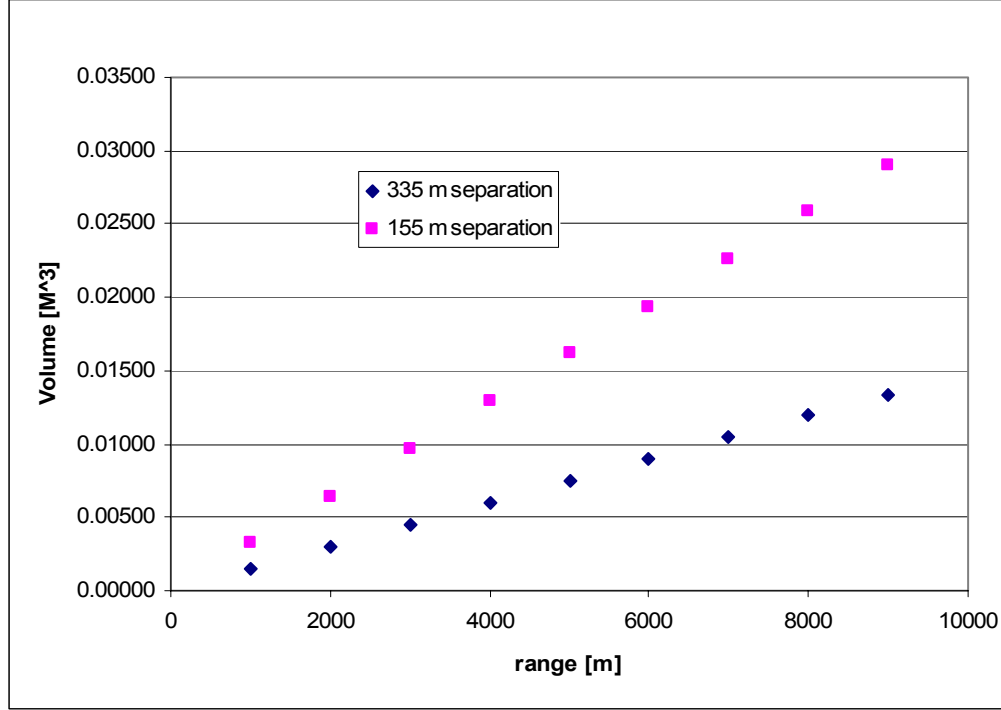


Figure 17. Overlap volume for two directors.

The largest volume is obviously at the longest range, where there is the most overlap. However, even this number is very small, 0.029 m³ for 155 m separation, and 0.013 m³ for 335 m.

As a comparison, the overall volume that one beam contains will be calculated. The formula for the volume of a tapered cylinder is

$$V = \frac{\pi l_t (r_s^2 + r_s r_t + r_t^2)}{3}, \quad (3.5)$$

where l_t is the range to target, r_s is the diameter of the beam director, and r_t is the beam radius at the target. Inserting the assumed values of $l_t = 8000\text{m}$, $r_s = 0.5\text{m}$, and $r_t = 0.05\text{m}$ yields an overall volume of 2320 m³. This means that the overlapped volume is a very small fraction of the overall volume of the beams.

Another consideration is the motion of the target. As was stated above, for fore-and-aft directors, there are only a few meters over which the beams overlap. Because of the motion of the target, however, this overlap does not stay in the same volume of air, so it will not heat sufficiently for blooming to occur. While the target moves, the air in the volume of the combined beams is constantly changing. A modest velocity for a cruise missile is approximately mach 0.8, or around 270 m/s. Obviously, it will cover this overlapped volume in a small fraction of a second, so there is little time for the air to heat enough to cause thermal blooming. Even for beams originating 2 m apart, the length of the overlapped portion of the beam path is on the order of 200 m at 8 km, so the volume of air where the beams are combined is refreshed in less than a second, which is still too short a time for thermal blooming to take effect. [14]

THIS PAGE INTENTIONALLY LEFT BLANK

IV. SIMULATIONS OF THE SHORT RAYLEIGH LENGTH FEL

Computer simulations are powerful tools for free electron laser developers. They allow researchers to vary parameters (e.g. electron beam current and energy, undulator wavelength, etc.) in order to optimize performance, understand operation, and determine what changes can be made in order to increase extraction and power, prior to actual construction. Also, they are helpful in showing the effects of various external stimuli on laser operation, such as mirror tilt and vibration. In this case, three dimensional simulations were used to study the effects of changing the number of undulator periods, the electron beam focus, the normalized Rayleigh length, and the mirror output coupling, as well as the effects of tilted resonator cavity mirrors.

The Rayleigh length is the characteristic distance over which the optical beam expands in area. Thus, shorter Rayleigh length means that the beam expands faster. Cavity mirrors can reflect only a certain amount of intensity before damage occurs. By using a short Rayleigh length, the mirrors can be closer together because the beam expands more quickly, so the power is spread over a greater area on the cavity mirrors in order to decrease the intensity. This is important because of the size limitations inherent in placing a FEL on a ship. Also, the focusing allows for amplification of a single optical wavefront, which greatly increases beam quality. [4] In Figure 18 below, the optical beam is outlined in blue, the electron beam in red, the undulator in green, and the magnetic field in black. The electron beam can also be focused in order to optimize the transfer of energy between the electrons and optical field.

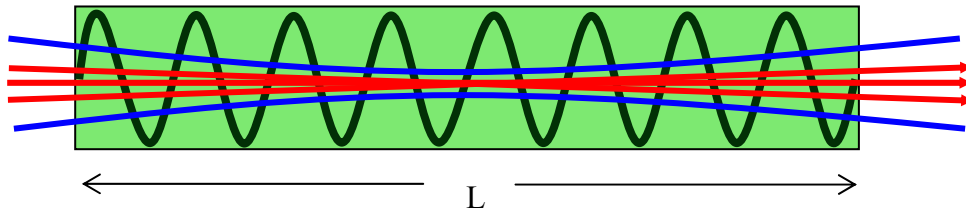


Figure 18. Optical and electron beam focusing in undulator.

There are two types of simulations that will be discussed, single-mode and multimode. For both types, the following parameters were used:

Undulator Parameters	
Number of Periods	$N = 14$
Length	$L = 37 \text{ cm}$
Wavelength	$\lambda_0 = 2.7 \text{ cm}$
Magnetic Field	$B = 0.8 \text{ T}$
Undulator Parameter	$K = 1.4$
Electron Beam	
Energy	$E_e = 100 \text{ MeV}$
Peak Current	$I_{\text{peak}} = 1500 \text{ A}$
Average Current	$I_{\text{avg}} = 1.1 \text{ A}$
Bunch Length	$l_b = 0.3 \text{ mm (1 ps)}$
Beam Focal Radius	$r_b = 0.07 \text{ mm}$
Emittance	$\epsilon_n = \gamma_0 r_b \theta_b = 9 \text{ mm/mrad}$
Focal Position	$z_b = 0.5L$
Angular Spread	$\theta_x = \theta_y = \theta_z = (\theta_x^2 + \theta_y^2)^{1/2} = 0.65 \text{ mrad}$
Optical Mode	
Wavelength	$\lambda = 1 \text{ }\mu\text{m}$
Resonator Length	$S \approx 16 \text{ m} - 20 \text{ m}$
Waist Radius	$w_0 = 0.09 \text{ mm}$
Spot Radius at Mirrors	$w = 3 \text{ cm}$

Table 1. Simulation parameters.

A. SINGLE-MODE SIMULATIONS

The equations for the averaged electron's motion are derived assuming that betatron focusing is small, and averaging over an undulator period to remove the fast wiggling motion [6]

$$x(z) = x_0 + \theta_x (z - z_b) \quad (4.1)$$

and
$$y(z) = y_0 + \theta_y (z - z_b), \quad (4.2)$$

where θ_x and θ_y are the injection angles for the sample electron, x_0 and y_0 are the initial offsets, and z_b is the location of the electron beam waist. This is illustrated by the red

lines in Figure 18 above, where not all of the electrons are injected on axis or at the same angle. The variable z is again the location along the undulator, as in Chapter II.

The optical field is assumed to be traveling in the z -direction with a Gaussian transverse profile, given by

$$E(r, z) = E_0 \left(\frac{\lambda z_0}{A} \right) e^{i(kz - \omega t + \phi)} e^{\frac{-\pi r^2}{A}}, \quad (4.3)$$

where

$$\phi(r, t) = -\tan^{-1} \left[\frac{(z - z_w)}{z_0} \right] + \frac{\pi r^2 (z - z_w)}{A z_0} \quad (4.4)$$

is the optical phase and

$$A = \lambda z_0 \left[1 + \frac{(z - z_w)^2}{z_0^2} \right] \quad (4.5)$$

is the optical mode area.

The evolution of the electron energy $E_e = \gamma mc^2$ along the undulator is given by

$$\gamma' = \frac{d\gamma}{dz} = \left(\frac{eK|E_e|}{\gamma mc^2} \right) [J_0(\xi) - J_1(\xi)] \cos(\zeta + \phi), \quad (4.6)$$

where J_0 and J_1 are Bessel functions, $\xi = K^2/2(1+K^2)$, and $\zeta = (k+k_0)z - \omega t$ is the electron phase as in Chapter II.

Integrating the electron phase with small integration steps $dz = cdt$, and noting that $\tau = ct/L$ so that $d\tau = (c/L)dt$ yields

$$\begin{aligned} \zeta' &= \frac{d\zeta}{dz} \\ &= \frac{d\zeta}{d\tau} \cdot \frac{d\tau}{dt} \cdot \frac{dt}{dz} \\ &= v \cdot \frac{c}{L} \cdot \frac{1}{c} \\ &= \frac{v_0 + \Delta v}{L} \end{aligned}$$

where $\nu = \nu_0 + \Delta\nu$ and $\Delta\nu \approx 4\pi N(\gamma - \gamma_0)/\gamma_0$, so that

$$\zeta'(z) = \frac{\left(\nu_0 + 4\pi N \left(\frac{\gamma - \gamma_0}{\gamma_0} \right) \right)}{L}. \quad (4.7)$$

The simulation is begun by setting the electrons' initial conditions: x_0 , θ_x , y_0 , θ_y , γ_0 , ζ_0 , and ν_0 . Using the equations of motion (equations (4.1) and (4.2)), the perpendicular positions of the electrons are found. From equations (4.3)-(4.5), the optical amplitude and phase are determined. Next, the electrons' energy exchange is found using equation (4.6), followed by the electron phase change from (4.7). When these steps are completed, the next iteration is begun using the updated numbers, and the process repeats.

Below is an example output of a single-mode simulation.

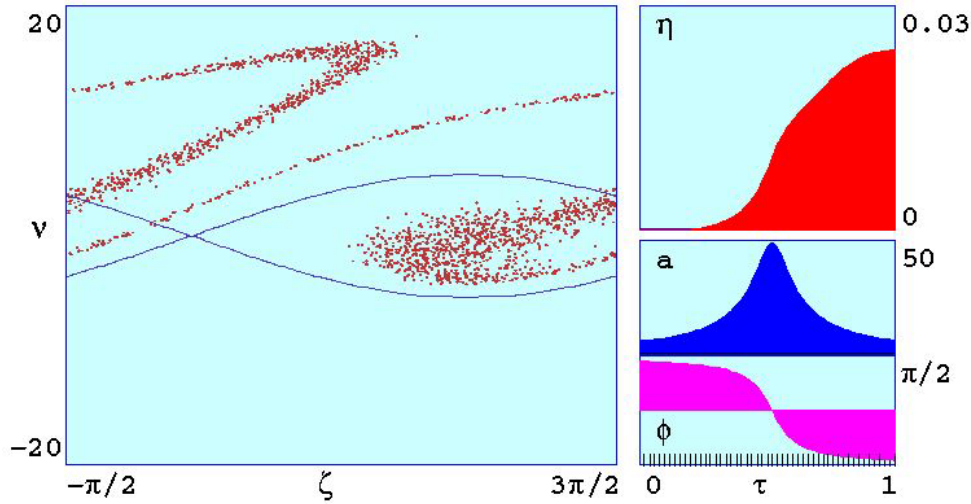


Figure 19. Single-mode simulation sample output.

The left side of Figure 19 is a phase space plot in (ζ, ν) similar to those shown in Chapter II, with the sample electrons shown as red dots and the separatrix shown in blue. This plot is the final state of the electrons at the end of the undulator, where the bunching of the electrons can be seen as well as the net decrease in phase velocity. The upper right of the figure shows the extraction, η , as the electrons pass through the undulator from $\tau = 0$ to 1. The middle right plot shows the evolution of the optical field strength, a . The peak at $\tau = 0.5$ shows the nature of the short Rayleigh length FEL, in that the optical field

is focused in the center of the undulator. The bottom right plot is the evolution of the optical field phase ϕ along the undulator.

B. MULTIMODE SIMULATIONS

Multimode simulations use the wave and pendulum equations derived in Chapter II of this thesis. An electron's longitudinal phase velocity is defined by equation (2.38), which again is

$$v = L \left[(k + k_0) \beta_z - k \right],$$

where L is the length of the undulator, $k = 2\pi/\lambda$ is the optical wave number, $k_0 = 2\pi/\lambda_0$ is the undulator wave number, and $\beta_z = v_z / c$. For off-axis electrons, this phase velocity is modified by,

$$\Delta v = -(\omega_\beta^2 y_0^2 + \theta_y^2), \quad (4.8)$$

where y_0 is the distance off-axis the electron is injected, $\omega_\beta = 2\pi NK/\gamma$ is the betatron frequency, and θ_y is the injection angle, as in the previous section. [3]

In multimode simulations, the optical wave equation is evaluated in three dimensions (x,y,t), evolving in space and time. The advantage of the multimode simulation over single-mode is that it includes multiple transverse optical modes and betatron motion, which is given by

$$y = (y_0 + \Delta y) \cos(\omega_\beta (\tau - \tau_\beta)) + \frac{\theta_{y0} + \Delta \theta_y}{\omega_\beta} \sin(\omega_\beta (\tau - \tau_\beta)), \quad (4.9)$$

where y_0 is the initial off-axis position of an electron, $\Delta \theta_{y0}$ is the initial tilt, Δy is a random shift due to the beam radial spread, $\Delta \theta_y$ is a random angle due to the beam angular spread, τ_β is the dimensionless position in τ of the beam focus, and τ is the dimensionless time as described in Chapter II. [2] It begins with weak fields, and evolves over many passes until steady-state power is reached.

Figure 19 below shows an output from a multimode short Rayleigh length simulation with $z_0 = 0.07$. The simulations use the dimensionless parameters discussed in Chapter II. The upper right section lists these parameters. In this case, the dimensionless current density $j = 150$ and a dimensionless radius in the x and y directions of $\sigma_{x,y} = 0.2$.

The electrons were injected with an initial phase velocity $v_0 = 11.25$. Both the electron beam and optical mode were focused at the center of the $N = 14$ period undulator, denoted by $\tau_\beta = \tau_w = 0.5$. The beam angular spread of $\sigma_{\theta x,y} = 0.7$ was determined by the betatron frequency $\omega_\beta = 0.6$ and the electron beam radius, and the Rayleigh length z_0 by the dimensionless mirror radius $r_m = 2.9$ and radius of curvature $r_c = 0.5$.

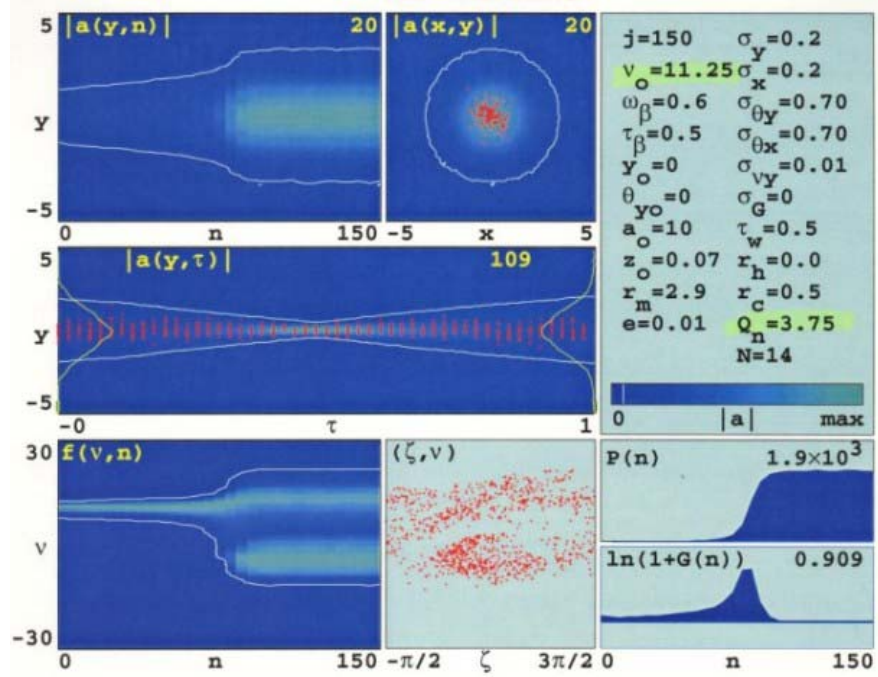


Figure 20. Multimode simulation output.

On the left-side of the figure, the upper and middle sections show the optical field intensity. The color scale is defined at the bottom of the parameter box, where dark to light blue represents low to high amplitude, respectively. Sample electrons are shown in red and the white contour lines delineate the 5% curve from the maximum optical field intensity at the cavity center. The upper-left plot shows the evolution of a cross-section of the optical field amplitude over $n = 150$ passes. The upper-center plot shows an end-on view of the optical mode at the end of the last pass.

The middle-left plot shows the side view of the cavity on the final pass. The sample electrons are shown in red, and the optical mode is shown using the same color scale as before. Here the focusing of the optical field can be seen, as well as the region of interaction with the electrons. The yellow line at each end of the figure represents the

profile of the optical field amplitude as it reaches the end of the undulator. In this case, in order to save run time, the simulation shows the beam only inside the undulator, from $\tau = 0$ to 1.

The bottom-left plot shows the evolution of the electron phase velocity over the $n = 150$ passes. The electrons are injected with an initial phase velocity $v_0 = 11.25$ and the phase velocity spread, and hence the energy spread, increases until the FEL reaches saturation at approximately 80 passes. The plot in the lower center shows the phase space distribution in (ζ, v) of the electrons at the end of the final pass, demonstrating electron bunching.

The two plots on the bottom right show the evolution of the wavefront power ($P(n)$) and gain ($\ln(1+G(n))$) as a function of the number of passes. The power plot shows again that steady state is reached at approximately 80 passes. In this case, $\eta \approx 3.8\%$ and the induced phase velocity spread was $\Delta v \approx 36$. The extraction is defined as

$$\eta(z) = \frac{\langle \gamma_0 - \gamma(z) \rangle}{\gamma_0} \quad (4.10)$$

where z is the distance along the undulator. [6]

C. SIMULATION RESULTS

Numerous single-mode and multimode simulations were conducted in order to study the effect of changing the undulator length, electron beam focus, normalized Rayleigh length, and output coupling, and the results of the two simulation techniques compared below.

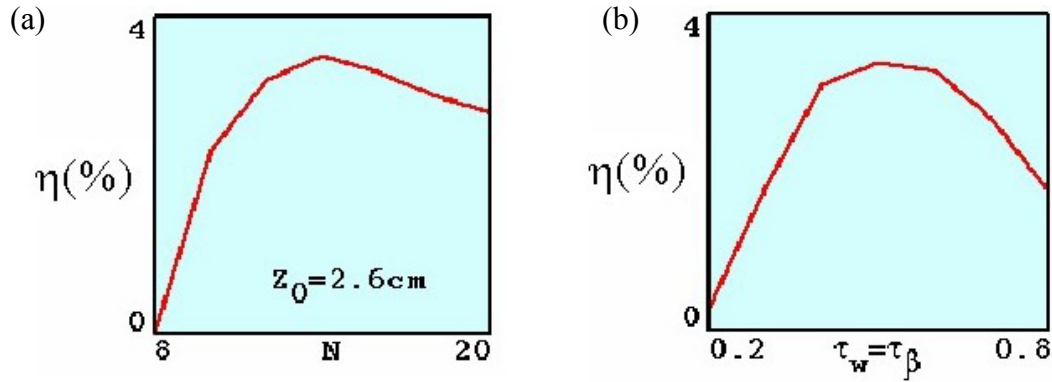
1. Variation of Undulator Length and Position

The first study was conducted in order to determine the effect of changing the number of undulator periods on extraction. The undulator wavelength was fixed at $\lambda_0 = 2.6$ cm and the number of periods varied from $N = 8$ to 20 periods. The FEL was below threshold for $N < 8$, so that there was no lasing. Figure 20(a) below shows the extraction as a function of the number of undulator periods for the single-mode simulation, while Figure 20(c) shows the results compiled from multimode simulations. As can be seen from the figures, the number of undulator periods plays an important role

in the extraction of the laser. It is interesting to note, however, that the ideal number of periods is around 14 for these parameters. Not only is there no advantage to having a longer undulator in a short Rayleigh length FEL, the extraction actually decreases slightly due to the electrons over-bunching. When this happens, electrons actually begin to take energy back from the optical mode. In phase space, this is shown by the electrons losing energy as in Figure 5 in Chapter II, but as they continue through the undulator, they continue to revolve clockwise. After they pass the minimum, they start increasing in energy, and are therefore taking energy back from the optical mode.

The difference in this case between multimode and single-mode simulations was slight. The peak in extraction in single-mode was $N = 14$, while the multimode yielded $N = 15$, both with a peak extraction $\eta \approx 3\%$. The decrease in extraction following this peak is more marked in the single-mode as well.

The other consideration that was addressed in the single-mode simulation is shown in Figure 20(b). This was the shifting of the undulator with respect to the electron beam and optical mode foci. The figure shows on the x-axis where the electron beam and optical mode were focused in terms of the dimensionless length of the undulator. It is shown that the ideal location for the foci is $\tau_w = \tau_\beta = 0.5$, or halfway along the undulator. The optical mode and electron beam foci will be varied independently in later sections.



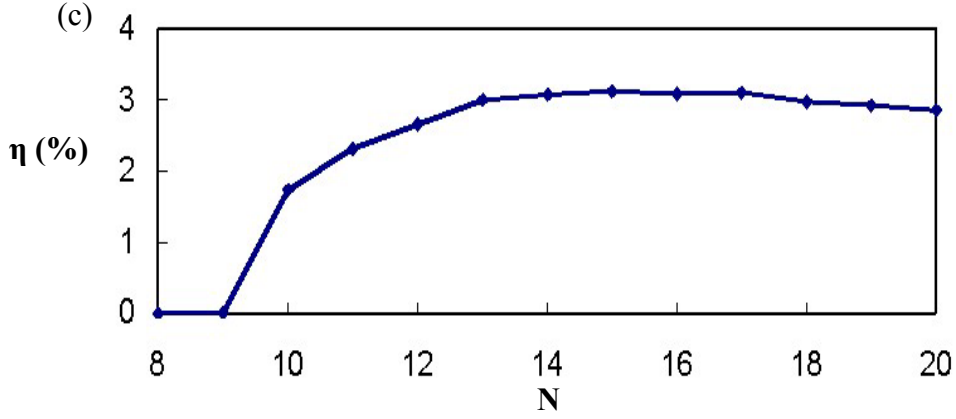


Figure 21. Results of varying undulator periods.

2. Variation of Electron Beam Focus

The next variation that was studied was the variation of the amount that the electron beam was focused. For this simulation, the normalized beam emittance, determined by the accelerator, was kept constant at $\varepsilon_n = \gamma r_b \theta_b \approx 9 \text{ mm-mrad}$, where r_b is the beam waist radius and θ_b is the divergence angle of the electron beam. With strong focusing, then the radius of the waist, r_b , is small, but θ_b is large. With weak focusing, the radius is large, and the spreading angle is small, as in Figure 22 below. This focusing of the electron beam results in an optimum value.

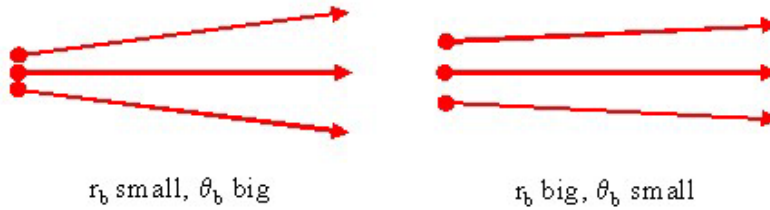


Figure 22. Pictorial representation of electron focusing.

The implication of this can be seen in Figure 23 below, which comes from multimode output files similar to Figure 19, where again the red is sample electrons and the white line the 5% curve from the maximum optical field intensity at the cavity center. With strong focusing, the electrons are contained entirely within the optical mode at the focus, but quickly expand outside of the optical mode, as in Figure 23(a). If the focusing is weak, then the waist radius will be larger than that of the optical mode, as in Figure 23(b). This is important because for optimal transfer of energy between the electrons and optical mode, the electrons must be within the optical mode.

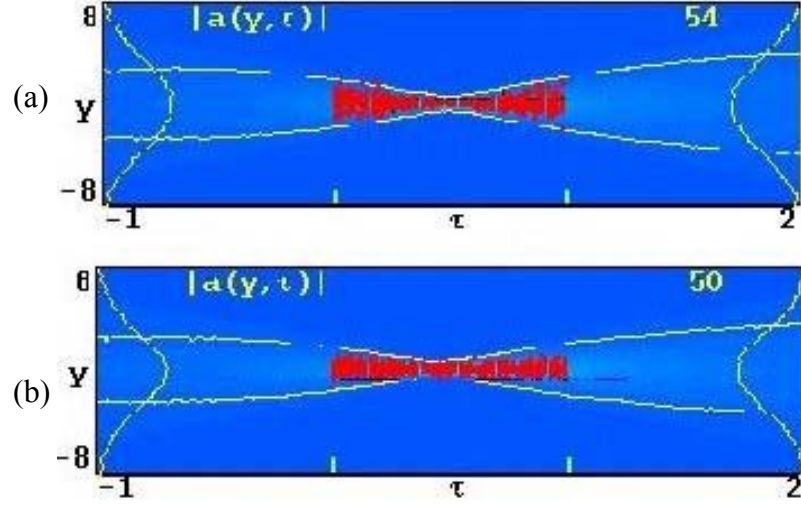
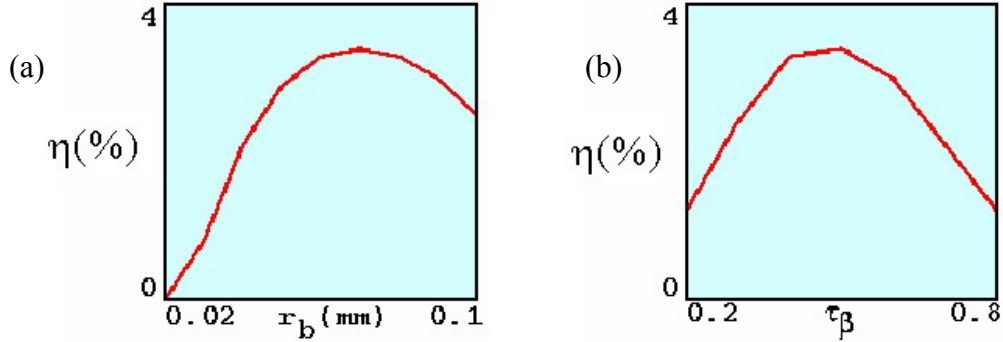


Figure 23. (a) Strong and (b) weak electron beam focusing.

Figure 24(a) below shows the extraction as a function of the optical beam waist radius, r_b , for the single-mode simulation. The extraction peaks because of the aforementioned conditions at $r_b = 0.07\text{mm}$ with a value of $\eta \approx 3.1\%$. The placement along the undulator of the electron focus was examined independent of the optical beam as well, and again found to be optimum near the center of the undulator, as shown in Figure 24(b). Figure 24(c) shows the result of the multimode simulations in which the dimensionless beam radius $\sigma = r_b (\pi / L\lambda)^{1/2}$ was varied. This results in $\sigma_{\text{max}} = 0.12$ ($r_b \approx 0.05\text{mm}$) with an extraction of $\eta = 3.8\%$.



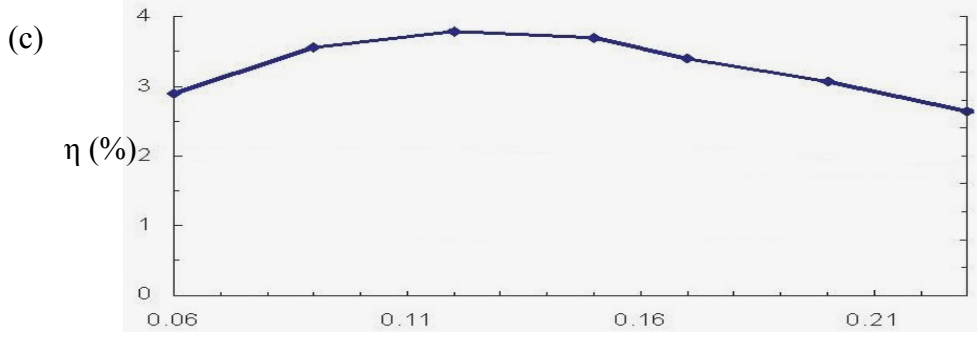


Figure 24. Variation of electron beam waist radius r_b .

3. Variation of the Rayleigh Length z_0

In this section, the effect of changing the Rayleigh length will be examined. The Rayleigh length was varied from $z_0 = 1.85$ cm to 4.44 cm with the cavity length constant, and the extraction η and mirror intensity I plotted in Figure 25(a) below in red and blue, respectively. The extraction steadily increases as the Rayleigh length is increased. However, the intensity on the mirrors quickly increases due to this increased extraction and the decreasing spot size. This means that the intensity quickly increases over the threshold which the mirrors can handle before failing. This level is assumed to be 200 kW/cm², and is shown as the horizontal green line on the figure. Therefore, the Rayleigh length should be kept at approximately 2.6 cm in order to avoid mirror damage while getting the maximum possible extraction. Figure 24(b) again shows the effect of changing the focus along the length of the undulator, this time moving the optical mode waist and keeping the electron beam focus at $\tau_\beta = 0.5$. The optimum location for the focus is again shown to be near half way along the undulator.

Figure 24(c) shows the result from the multimode simulations. In this case, the normalized Rayleigh length, which is normalized to the length of the undulator, was varied. Due to mirror considerations listed above, the normalized Rayleigh length should be approximately 0.06, or 2.3 cm.

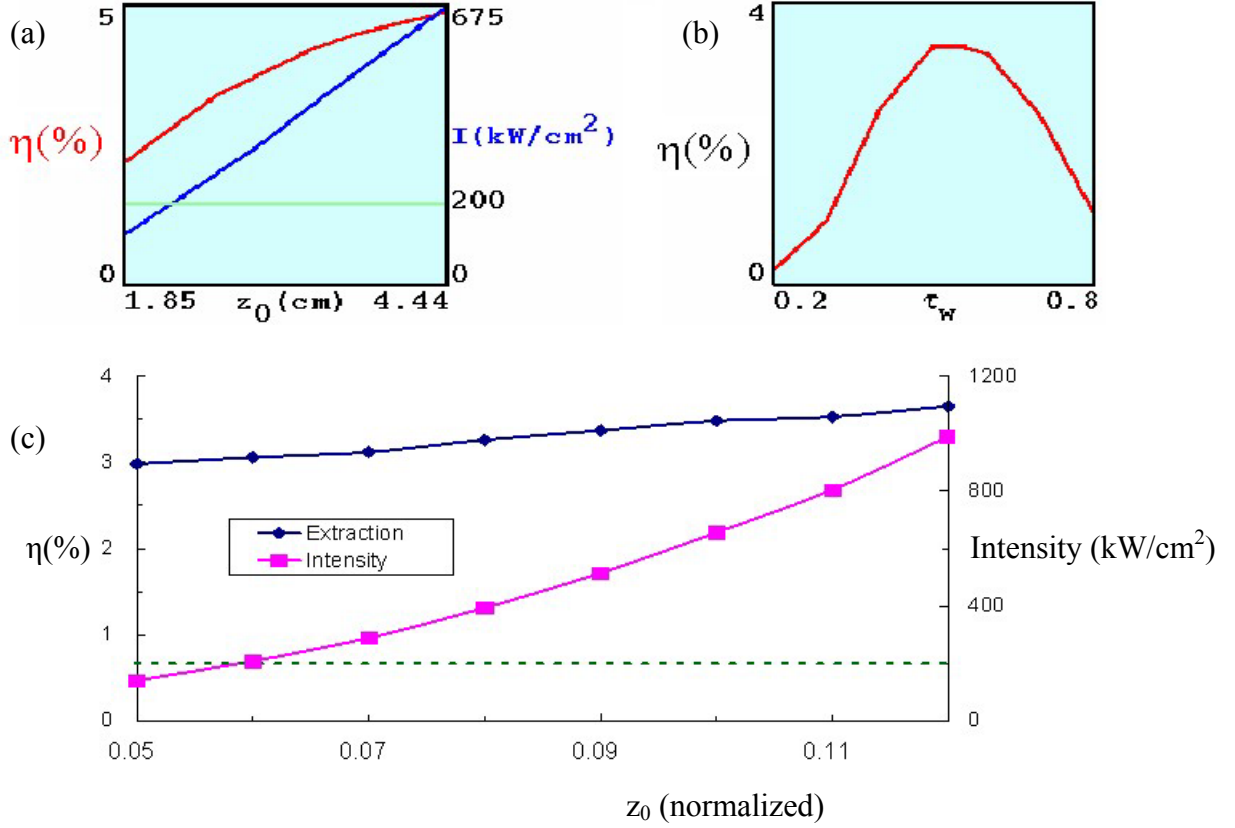


Figure 25. Variation of the Rayleigh length.

4. Variation of Mirror Output Coupling Q_n

The last parameter that was varied in both single-mode and multimode simulations was the output coupling. This represents the amount of energy that the partially transmissive mirror reflects every pass. The variable in Figure 25 below, Q_n , is defined as the inverse of the output coupling. For instance, for $Q_n = 2$, there is 50% output coupling, or 50% transmission of the power. As expected, the extraction increases as the output coupling decreases, which can be seen in Figure 26(a) and the blue line in (c). This is due to the fact that stronger optical fields within the undulator extract more energy from the electrons. However, as was mentioned in the previous section, there is a limit on the amount of intensity that the mirrors take before suffering damage. Figure 26(b) below shows the power contained within the cavity as a function of the output coupling for the single-mode simulation, and is given by $P_{\text{in}} = Q_n P_{\text{out}}$. The pink line in Figure 25(c) shows the intensity on the mirrors as a function of Q_n in the multimode

simulation. The green line in both plots again represents the 200 kW/cm² intensity limit for the mirrors. In the single-mode simulation, P_{in} rapidly increases with Q_n and exceeds the mirror damage threshold at a Q_n of approximately 2. In the multimode simulation, it exceeds this damage threshold at a slightly lower value.

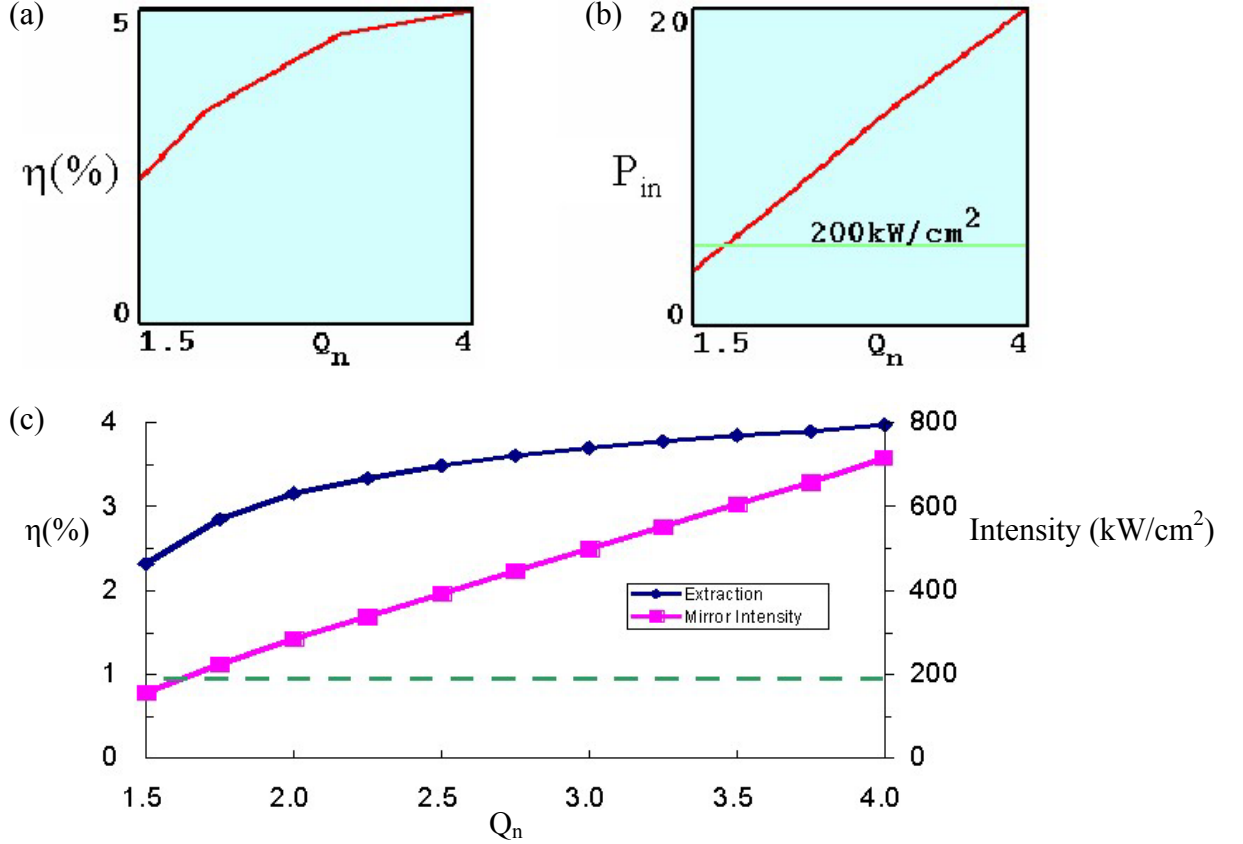


Figure 26. Variation of mirror output coupling Q_n

D. MIRROR TILT

A separate set of multimode simulations was conducted in order to determine the effect of mirror tilt on short Rayleigh length FEL's. Specifically, the extraction will be shown for cavity mirrors tilted from $\theta_m = 0 \rightarrow 0.5$ with a normalized Rayleigh length of 0.1. The tilt angle θ_m is the normalized tilt angle, and is defined as $\theta_m = \theta / (\lambda/L\pi)^{1/2}$. Other Rayleigh lengths were studied, but $z_0 = 0.1$ was the most instructive for studying larger angles due to limitations of the window size within the simulation. Another interesting aspect that will be addressed is the effect that mirror tilt has on the optimal v_0 , which will be discussed later in this section.

1. Extraction Decrease Due to Beam Tilt

As can be seen in the figure below, the effect of tilting the resonator cavity mirrors is that the interaction region between the optical field and the electron beam is not centered throughout the entire length of the undulator. This means that the electrons are not seeing the strongest optical fields possible, so that the extraction decreases. The greater the mirror tilt, the shorter the interaction region, and therefore the weaker the extraction.

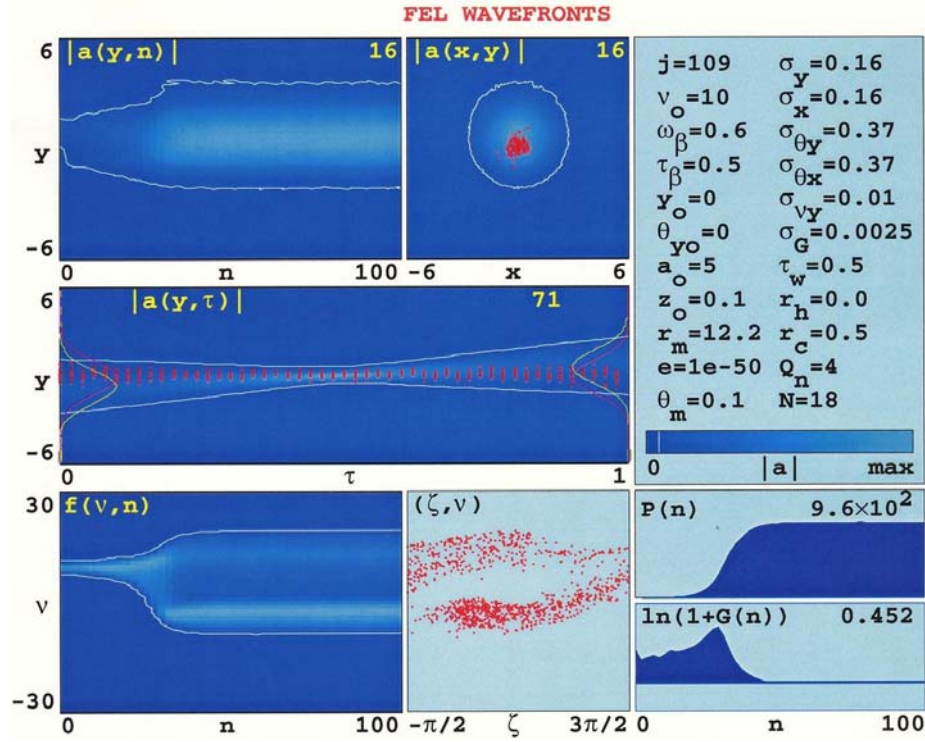


Figure 27. Multimode simulation run with tilted mirrors.

Figure 28 below shows the results of the runs conducted to study the effect of the mirror tilt for a normalized Rayleigh length of $z_0 = 0.1$. As can be seen in the figure, increasing the mirror tilt θ_m causes the extraction η to decrease. However, it is worth noting that the extraction remains over 1% for a mirror tilt $\theta_m = 0.50$. This corresponds to an actual mirror tilt of $\theta \approx 0.4 \mu\text{rad}$. With active alignment, however, it is anticipated that design tolerances will be on the order of $0.1 \mu\text{rad}$, so that the effect on extraction due to this vibration will be minimal. [7]

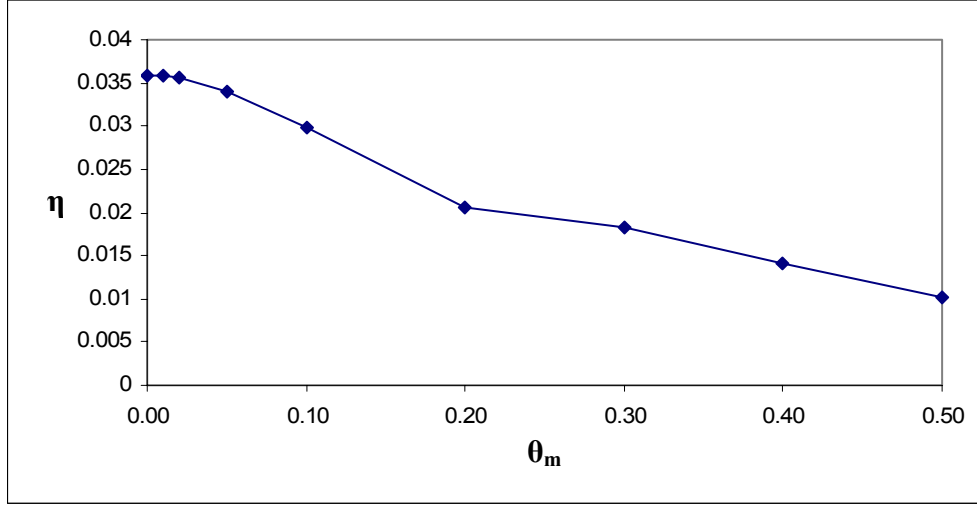


Figure 28. Extraction decrease due to mirror tilt.

2. Mode Shape

Another interesting aspect of mirror tilt is the effect on the optimum value for v_0 and the mode shape. In practice, FEL's automatically progress to the most efficient value of v_0 at steady state for the given parameters. In our multimode simulations, that value must be found manually. Iterations of v_0 are conducted and the maximum extraction found, which is what is plotted in graphs such as Figure 27 above.

For simulations that do not involve mirror tilt, as v is increased the extraction increases smoothly to a maximum, and then drops sharply. In running the simulations for this study, however, there was found to be dual peaks instead. Both of these are shown in Figure 28 below, in which the non-tilted mirror ($\theta_m = 0$) is shown in blue and the tilted mirror ($\theta_m = 0.01$) in red.

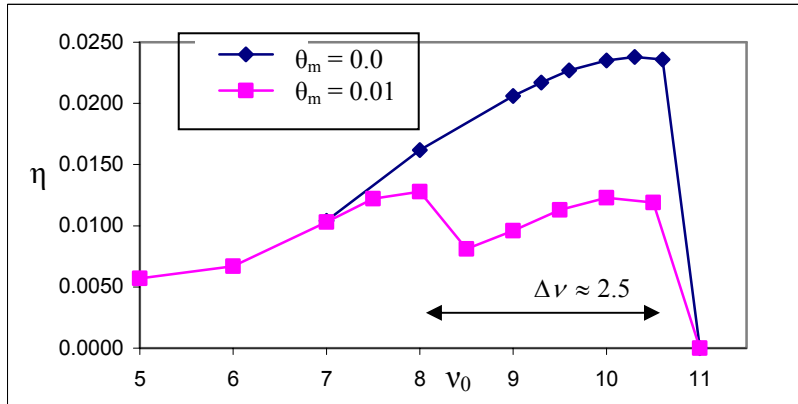


Figure 29. Example of finding maximum extraction varying initial electron phase velocity.

This is due to the changes in the optical mode shape as the mirror is tilted. With no mirror tilt, the short Rayleigh length FEL typically operates in the fundamental Gaussian mode. With the mirrors tilted, this mode becomes distorted, with side lobes appearing. The amplitude of these side lobes increase with increasing ν_0 until they reach a maximum, shown Figure 30(a) below, which shows the optical mode amplitude profile at the cavity center. As ν_0 continues to increase, however, the side lobes are absorbed into the main peak, as can be seen in Figure 30(b). When this new mode begins, the extraction drops. As ν_0 continues to increase, the extraction increases to a second maximum, and the optical mode becomes the more familiar Gaussian, as in Figure 30(c). This increasing ν_0 also corresponds to an increase in FEL operating wavelength.

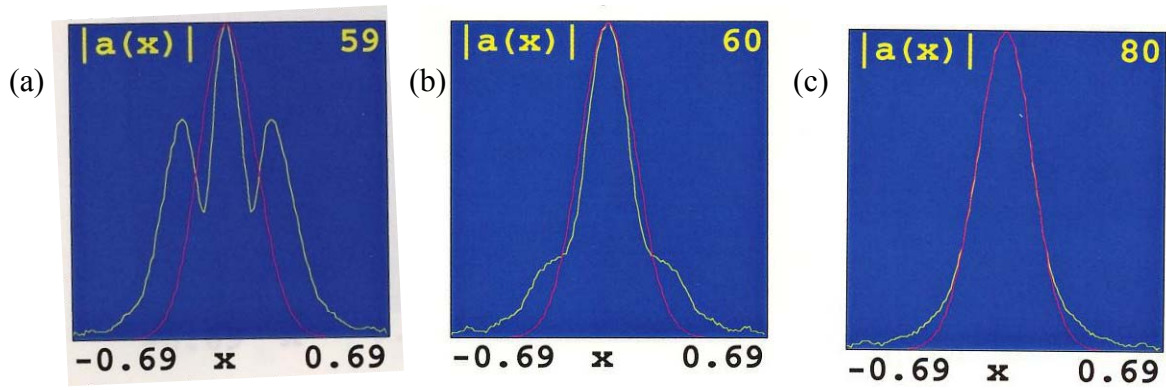


Figure 30. Optical mode profiles for $z_0 = 0.03$, $\theta_m = 0.01$, and $\nu_0 =$ (a) 8.0, (b) 8.5, and (c) 10.

In the case shown in Figure 29, the FEL evolves from the “triple hump” mode at $\nu_0 \approx 8$ to the Gaussian mode at $\nu_0 \approx 10.5$. Knowing $\Delta\nu$, the change in wavelength can be found. Equation (2.38) gave

$$\nu = L[(k + k_0)\beta_z - k].$$

Substituting the definition $k = 2\pi/\lambda$ yields

$$\nu(\lambda) = \frac{2\pi}{\lambda} L\beta_z + k_0 L\beta_z - \frac{2\pi}{\lambda} L. \quad (4.11)$$

Taking the change in ν as a function of λ yields

$$\frac{\Delta\nu}{\Delta\lambda} = -\frac{2\pi\beta_z L}{\lambda^2} - \frac{2\pi L}{\lambda^2} \quad (4.12)$$

$$\frac{\Delta \nu}{\Delta \lambda} = 2\pi L(1 - \beta_z). \quad (4.13)$$

Equation (2.28) showed that

$$\beta_z \approx 1 - \frac{1 + K^2}{2\gamma^2}$$

and equation (2.16)

$$\lambda = \lambda_0 \frac{1 + K^2}{2\gamma^2}.$$

Combining these two yields

$$\beta_z = 1 - \frac{\lambda}{\lambda_0}. \quad (4.14)$$

Inserting equation (3.19) into (3.18) yields

$$\frac{\Delta \nu}{\Delta \lambda} = \frac{2\pi L}{\lambda^2} \left(1 - 1 + \frac{\lambda}{\lambda_0} \right) \quad (4.15)$$

so that

$$\Delta \nu = \frac{2\pi L}{\lambda_0} \frac{\Delta \lambda}{\lambda}. \quad (4.16)$$

Since $L = N\lambda_0$, then equation (3.21) can be written as

$$\frac{\Delta \lambda}{\lambda} = \frac{1}{2\pi N} \Delta \nu. \quad (4.17)$$

For $N = 18$ and $\Delta \nu \approx 2.5$, equation (3.22) shows that the wavelength change in the FEL due to this transition is approximately $\Delta \lambda / \lambda \approx 2.2\%$.

THIS PAGE INTENTIONALLY LEFT BLANK

V. CONCLUSION

The free electron laser is a promising new weapon system that will change the face of modern warfare. Speed of light delivery of energy on target, deep magazines, low cost-per-shot, and pinpoint accuracy offer significant advantages over current weapon technologies. Although the current concentration for FEL applications is on ship self defense, there are numerous other applications mentioned in the introduction of this thesis, and undoubtedly others that will be realized once it is implemented in an operational environment.

Simulations conducted by the Directed Energy and Electric Weapons Center at the Naval Postgraduate School show that a short Rayleigh length is an important configuration for a compact, weapons grade FEL to reduce intensity on mirrors in the resonator cavity. Due to the limited space allowed for a weapon system, the shorter resonator cavity lends itself to ship-board implementation. The simulations conducted for the 2003 International Free Electron Laser Conference in Tsukuba, Japan, which have been incorporated into this thesis, define some of the parameters necessary for next generation FELs. Optimal values for parameters such as the number of undulator periods, electron beam focus, the normalized Rayleigh length, and mirror output coupling were determined. Simulations were also conducted in order to examine the effect of mirror tilt on laser power and extraction. This demonstrated the importance of accurate simulations, in that the effect of varying parameters can be determined in order to help scientists and engineers develop future systems, and comparison between the single-mode and multimode simulation techniques contributed to validating the results. Simulations also aid greatly in understanding how FEL parameters interact.

Multiple beam directors, already proposed for maximum radial coverage, can mitigate thermal blooming. The power limitations caused by thermal blooming can be a significant factor in the implementation of high-power lasers. The use of multiple directors will allow for more power to travel through the atmosphere because each individual beam will be below the threshold of thermal blooming, while the combined intensity on target still meets the desired specifications. The study conducted in this

thesis quantifies the effects of beam director separation on thermal blooming, and shows that this is a viable option for the reduction of thermal blooming.

Directed energy weapons promise to revolutionize modern warfare. The results of this thesis show how a free electron laser can be designed and deployed on a ship for use as a defensive weapon, addressing key issues such as mirror damage, cavity stability, and thermal blooming.

LIST OF REFERENCES

- [1] Benson, Stephen V. "Free Electron Lasers, Push Into New Frontiers." *Optics and Photonics News*, May, 2003.
- [2] Blau, J.; Bouras, V.; Kalfoutzos, A.; Allgaier, G.; Fontana, T.; Crooker, P.P.; Colson, W.B. "Simulations of High-Power Free Electron Lasers With Strongly Focused Electron and Optical Beams." *Nuclear Instruments and Methods in Physics Research, A507*, pp 44-47.
- [3] Colson, W.B. "Classical Free Electron Laser Theory." *Free Electron Laser Handbook*. The Netherlands: Elsevier Science Publishing Co. Inc, 1990. Chapter 5.
- [4] Colson, W.B., J. Blau and R.L. Armstead. "The Free Electron Laser Interaction with a Short-Rayleigh-Length Optical Mode." (2003)
- [5] Colson, W.B., PH4911 class notes (2003)
- [6] Colson, W.B., J. Blau, R.L. Armstead, and P.P. Crooker. "Single Mode Simulations of a Short-Rayleigh Length FEL." Submitted at International Free Electron Laser Conference in Tsukuba, Japan, 2003.
- [7] Crooker, P.P.; Campbell, T.; Ossenfort, W.; Miller, S.; Blau, J.; Colson, W.B. "A Study of the Stability of a High-Power Free Electron Laser Utilizing a Short Rayleigh Length." Submitted at International Free Electron Laser Conference in Argonne, IL, 2002.
- [8] Fontana, Tim. "High Power Optical Cavity Design and Concept of Operations for a Shipboard Free Electron Laser Weapon System," Master's Thesis, December, 2003.
- [9] Jackson, John David, *Classical Electrodynamics*, 2nd Edition, New York, NY, 1975.
- [10] J. Blau, G. Allgaier, S. Miller, T. Fontana, E. Mitchell, B. Williams, P.P. Crooker, and W.B. Colson, "Multimode Simulations of a Short-Rayleigh Length Free Electron Laser," Submitted at International Free Electron Laser Conference in Tsukuba, Japan, 2003.
- [11] Murphy, J.B. "Energy Recovery LINACs Light Sources: An Overview." *Proceedings of the 2003 Particle Accelerator Conference*.
<http://epaper.kek.jp/p03/PAPERS/TOAC001.PDF>, (11 Feb 04)

- [12] Neil, George R. “High Power FELs Driven by RF Superconducting LINACs.” <http://laacg1.lanl.gov/rfsc99/FRA/fra002.pdf>, (10 Feb 04)
- [13] Solid State Division of RCA, Inc., *Electro-Optics Handbook*, (1974)
- [14] Email correspondence between Robert D. Stock, Lincoln Labs, MIT, and the author, 12 Feb 04.

INITIAL DISTRIBUTION LIST

1. Defense Technical Information Center
Ft. Belvoir, Virginia
2. Dudley Knox Library
Naval Postgraduate School
Monterey, California
3. Professor William B. Colson, Code PHCW
Department of Physics
Monterey, California
4. Professor Joseph Blau, Code PHBL
Department of Physics
Monterey, California
5. Professor Peter Crooker, Code PHCP
Department of Physics
Monterey, California
6. Professor Robert L. Armstead, Code PHAR
Department of Physics
Monterey, California
7. Chairman, Physics Department, Code PHMW
Naval Postgraduate School
Monterey, California
8. Engineering and Technology Curricular Office (Code 34)
Naval Postgraduate School
Monterey, California
9. CAPT Roger McGinnis, USN
Naval Sea Systems Command
CODE SEA 53R
Washington D.C.
10. Dr. George Niel
TJNAF
Newport News, Virginia
11. Dr. Steve Benson
TJNAF/MS6A
Newport News, Virginia

12. Dr. Fred Dylla
TJNAF
Newport News, Virginia
13. Dr. Alan Todd
Advanced Energy Systems
Princeton, New Jersey
14. Dr. Gil Graff
Office of Naval Research, Code 531
Arlington, Virginia
15. Michael B. Deitchman
Office of Naval Research, Code 531
Arlington, Virginia
16. LT Ethan D. Mitchell, USN
Surface Warfare Officer School
Newport, Rhode Island